

Analysis of Soil-Tire Interaction
Using a Two-Dimensional
Finite Element–Discrete Element Method

2019

Kenta Nishiyama

Acknowledgements

First, I would like to express my deep gratitude to the supervisor of this dissertation, Professor Hiroshi Shimizu, Laboratory of Agricultural Systems Engineering (LASE), Kyoto University, whose insightful comments and suggestions were of great benefit for this study, and would like to thank him for reviewing the dissertation. I would also like to sincerely thank another member of my dissertation committee, Professor Michihisa Iida, Laboratory of Field Robotics, for his constructive suggestions and keen discussion of the dissertation.

I would also like to appreciate the efforts of Associate Professor Hiroshi Nakashima of LASE, a member of my dissertation committee, who has continuously advised me during this study, which originated from my undergraduate thesis and continued throughout my master's thesis in the Group of Terramechanics, LASE. I also wish to express my gratitude to Assistant Professors Juro Miyasaka and Katsuaki Ohdoi of LASE for their meticulous and constructive comments during the laboratory seminars.

Part of this study, which is presented in Chapter 5, was supported by JSPS KAKENHI Grant no. 23580359, held by Dr. Hiroshi Nakashima. The experimental results for elastic wheels described in Chapter 3 were supplied by Dr. Lutz Richter, a former head of the Department of Exploration Systems, DLR Bremen, Bremen, Germany. We would like to thank Dr. Marco Scharringhausen of DLR Bremen, who was in charge of the experiments, for his comments and advice related to the experimental data. We also wish to acknowledge a former graduate student, Mr. Yuzuru Takatsu, who prepared the FE-DEM code framework.

I would like to also express my gratitude to the Digital Solution Center, Bridgestone Corporation, for their support and encouragement.

Finally, I would like to express my heartiest thanks to my wife, Anna, for her understanding and encouragement, and my son, Atsuhiko, for his patience during the manuscript writing stage, without which this dissertation could not have been accomplished.

Table of Contents

Acknowledgements	i
1 Introduction	1
1.1 Background	1
1.1.1 Semi-empirical method in terramechanics	2
1.1.2 Computational method in terramechanics	2
1.2 Purpose of the study	4
1.3 Outline of the dissertation	4
References	5
2 Overview of FE–DEM	9
2.1 Introduction	9
2.2 Formulation of FE–DEM	10
2.3 Numerical integration method	11
2.3.1 FEM	11
2.3.2 DEM	12
2.4 Tractive performance analysis of a tire using FE–DEM	12
2.5 Contact reaction	13
2.6 Program flow	15
References	16
3 Tractive performance of an elastic wheel for planetray rovers	19
3.1 Introduction	19
3.2 FE-DEM analysis of wheel performance	19
3.2.1 Updated traction analysis	19
3.2.2 Structure of the wheel model and parameters	23
3.3 Results and discussion	27
3.3.1 Results of numerical analysis	27
3.3.2 Discussion	32
3.4 Prediction of wheel performance on Mars using FE–DEM	35

3.5	Conclusion	38
	References	39
4	Contact stress and tractive performance of a tire driven on dry sand	41
4.1	Introduction	41
4.2	Traction performance analysis	42
4.2.1	Traction performance analysis using a model incorporating FE–DEM with PID control	42
4.2.2	Normal and tangential contact stresses in FE–DEM	43
4.2.3	Tractive performance analysis using a parametric approach	45
4.2.4	Input parameters in FE–DEM analysis	46
4.3	Results and discussion	49
4.3.1	Soil behavior under a traveling tire	49
4.3.2	Normal and tangential contact stresses	50
4.3.3	Angle of rotation for maximum contact reaction	51
4.3.4	Tractive performance	53
4.3.5	Contact load	54
4.4	Conclusion	55
	References	55
5	FE-DEM with interchangeable modeling for traction analysis	57
5.1	iFE-DEM: FE-DEM interchangeable model	57
5.1.1	Outline of iFE-DEM	57
5.1.2	Conversion from FEM to DEM	58
5.1.3	Conversion from DEM to FEM	60
5.1.4	Attached discrete elements on the border of finite element after tire travel	61
5.1.5	Preparation of discrete elements for conversion from FEM to DEM	63
5.1.6	Confined compression test for determining Young’s modulus of soil FEM	64
5.1.7	Tractive performance	65
5.2	Numerical experiment	65
5.2.1	FE-DEM parameters	65
5.2.2	Program flow for iFE-DEM	68
5.3	Results and discussion	69
5.3.1	Soil deformation under tire travel	69
5.3.2	Tractive performance	70
5.3.3	Computational load in iFE-DEM	72
5.3.4	Stress distribution within soil model in iFE-DEM	73
5.4	Conclusion	74

TABLE OF CONTENTS

v

References 76

6 Conclusions **77**

Chapter 1

Introduction

1.1 Background

Soil-tire system interaction is one of the fundamental research subjects in terramechanics. In off-road vehicles, such as agricultural and construction machinery, soil-tire interaction is the dominant factor for tractive performance and working productivity. It has been empirically established that the tractive performance of a tire can be improved by reducing its inflation pressure, which results in a larger contact area, low sinkage, and low running resistance of the tire derived from increased tire deflection. Using tractor tires with a low inflation pressure, soil compaction by farm tractors can be avoided in agricultural fields, in order to allow optimal growth of plant roots. Off-road vehicles with superior performance (lightweight, reduced fuel consumption, increased working capacity, etc.) can be developed if the tires' performance is predicted beforehand in the design and development process.

Furthermore, small autonomous rovers have been studied and developed in several countries in recent years for exploring extraterrestrial surfaces on the Moon and on Mars. These rovers should have enough capability to travel over the regolith, which consists of fine dusty particles covering the surfaces of planets. Owing to the payload limitation of rockets, the wheels of a rover should be simple and compact in design, with sufficient tractive performance to maneuver weak surface conditions. However, the tractive performance of rover wheels cannot be evaluated by in-situ experiments; instead, it should be estimated on Earth in a highly sophisticated experimental facility with high vacuum, where acceleration due to gravity can be controlled. Therefore, developing a tool for predicting the wheel performance accurately under reduced gravity conditions has become necessary.

In addition to the experimental approach, there are two other major approaches for predicting soil-tire system interactions. The first one is the semi-empirical method, and the second approach comprises computational methods, such as the finite element method (FEM) and distinct or discrete element method (DEM).

1.1.1 Semi-empirical method in terramechanics

The semi-empirical method was originally proposed by M. G. Bekker [3, 4]. In this method, a contact interaction on the soil-tire interface is assumed to be expressed by two characteristic relationships: (i) the pressure-sinkage (PS) relationship and (ii) shear stress-shear displacement (SS) relationship. The PS relationship is assumed to contribute to the motion resistance, whereas the SS relationship is assumed to contribute to the gross tractive effort, or thrust, in the traction performance of off-road tires. The SS relationship was further simplified as the Janosi-Hanamoto (JH) equation to consider soft deformable cohesive soils [9]. The governing parameters of the PS and SS relationships can be measured using a bevameter, which stands for “Bekker Value Meter” [4]. The bevameter is a measuring device system where each PS relationship and SS relationship can be measured. Based on the two obtained relationships, Bekker predicted the compaction resistance (or motion resistance) of a crawler on soil by assuming a rigid footing of the crawler [3]. Similarly, the compaction resistance of a rigid tire was also formulated once the shape of the contact surface was considered [3].

Subsequently, Wong refined Bekker’s approach as a parametric approach, whereby he developed a computational tool for evaluating the performance of off-road vehicles on the basis of Bekker’s two relationships [28, 29]. After the soil parameters in the PS and JH relationships are obtained, the normal and tangential contact stresses distributed over the contact length can be calculated. Moreover, the tractive performance of an off-road vehicle can be derived from the numerical integration of normal and tangential stresses over the contact surface of a crawler or tire once the specification of the vehicle and its operating condition parameters are input. Since the parametric approach is quite simple, this method has been popular and is applied even now [6, 13, 24]. In general, this method has a low computational cost; however, it is not very accurate because the PS relationship assumes a function of sinkage, where the maximum pressure may occur at the maximum sinkage of the plate, which is not true for the locomotion of off-road tires with slip and sinkage.

1.1.2 Computational method in terramechanics

Owing to the recent developments in information technology, there has been an increase in the possibility of numerical simulations applied to interaction problems in terramechanics. Among others, FEM and DEM are candidate tools.

Fundamentally, FEM, which is adequate for continuum models, has been applied in the research and development of wheels for off-road vehicles. In terms of numerical analysis, soil-tire system interactions have traditionally been analyzed using the FEM with a simplified and approximate boundary condition [31, 32]. The introduced soil model was not only elastic, but also elasto-plastic. Ueno et al. [27] applied the elasto-plastic soil model and a contact algorithm for the analysis of a two-dimensional (2D) soil-wheel system. Hiroma et al. [8] analyzed rigid wheel-viscoelastic soil interactions using FEM with a contact algorithm, where the wheel surface was assumed to be

smooth. Developments can also be seen in the application of critical state soil mechanics to tire-soil problems [12]. With the further development and refinement of FEM, an in-depth analysis of contact problems has been formulated, as summarized in a book [33]. Since the interaction problems in terramechanics belong to typical contact mechanics in nature, the application of the achievements from contact mechanics becomes important in computational terramechanics for soil-tire systems. Aubel [1] successfully analyzed the 2D interaction between a soft soil and an elastic rolling smooth tire. Furthermore, Fervers [7] extended and demonstrated a treaded tire-soil interaction analysis using FEM. Some reports described examples of soil-wheel interactions using FEM [7, 22, 23, 25, 30, 32]. However, the effect of a tread pattern or lugs on the tractive performance of wheels have been a challenging topic in applications of FEM to soil-wheel systems.

On the other hand, DEM, which was originally proposed by Cundall and Strack [5], has been applied not only to soil or rock mechanical problems, but also to simple tillage and wheel-soil interaction problems. A typical soil model using DEM consists of an assembly of discrete granular elements and can be simply implemented as a computer program. Oida et al. [20] demonstrated for the first time the applicability of DEM to a wheel-soil contact problem, where various wheel lugs were considered. It should be noted that the wheel rut usually observed in outdoor experiments can be similarly obtained using DEM [20]. However, DEM is more appropriate than FEM for the analysis of interactions such as soil and wheel lugs [2, 10, 11, 15, 16, 26]. While applications of DEM to three-dimensional (3D) problems have become more common in recent years [10, 11, 26], the computational load associated with 3D DEM is still a big challenge when the total number of discrete elements is increased. It was noted that the element shape in DEM plays an important role in the analysis of the soil behavior. Simply shaped circular (2D) or spherical (3D) elements have been used in DEM; however, introducing an additional rolling resistance moment becomes necessary to prevent excessive element rotation. In recent years, the use of other elemental shapes, such as ellipsoids [11] and clumped elements [10, 14], has become popular with the availability of high-performance computing. However, the increased computational time caused by the contact check and contact reaction calculation using a small increment of the time step in the numerical integration of numerous discrete elements is a well-known bottleneck affecting DEM.

Thus, a new coupled methodology is expected, where the smaller influential soil region under the soil-tire contact interaction is analyzed using DEM, whereas the other noninfluential soil region and tire are analyzed using FEM. In this study, such a combined methodology is named the finite element–discrete element method (FE–DEM). Using FE–DEM, the analysis of soil-tire interactions can become less time-consuming because of the reduced soil region of DEM, while it can realize the soil behavior under the action of a tire with lugs similar to when only DEM is applied. FE–DEM is explained in Chapter 2 in more detail.

1.2 Purpose of the study

The ultimate goal of this study is to develop a prediction tool for the tractive performance of a tire or a wheel traveling on soil. In order to achieve this goal, we aim to develop a new framework of FE–DEM for estimating the tractive performance of a tire on dry sand with a high accuracy. The existing 2D FE–DEM code developed by our research group was updated to improve the accuracy of analysis specifically for deformable tire conditions. In this study, we consider 2D analysis because the validity of the proposed algorithm for FE–DEM should be evaluated using a simple computer implementation. To evaluate the framework's accuracy, numerical results are compared to the results of an experiment, in which tractive forces and wheel sinkage against the slip ratio were assessed.

Another purpose of this study is to propose a new way of reducing the computational cost of DEM. The effect of reducing the elapsed computational time will be discussed with respect to the size of the DEM region.

1.3 Outline of the dissertation

Chapter 2 presents a review of FE–DEM together with its fundamental formulations, the contact model between FE and DE, the traction performance calculated from the FE–DEM program, and the description of its program flow.

In Chapter 3, an analysis of the tractive performance of an elastic wheel for planetary rovers is presented [17]. The wheel traveling control method is improved to represent the experimental condition, and the proposed algorithm is applied to the analysis of a metallic small elastic wheel prototype, which is intended to be equipped for a Mars exploration rover. In order to simulate the forced-slip condition in the experiments, a proportional-integral-derivative (PID) controller model of the tire position and rotation activated by the drawbar pull and wheel torque is introduced in the FE–DEM simulation. Wheel rigidity varied using the Young's Modulus and the gravity effect are investigated.

Chapter 4 presents an analysis of the contact stress and tractive performance of a tire driven on dry sand, as stated in [18]. Normal and tangential stresses acting over a contact interface of a tire driven on dry sand are investigated in order to expand their applicability. A simple averaging method for contact reaction is introduced, assuming that the tire is in the rigid contact mode and would travel on the model sand terrain in the stationary condition. The tractive performance calculated from the contact stresses using a semi-empirical (or parametric) approach is compared with the result directly obtained from FE–DEM.

Chapter 5 presents FE–DEM with interchangeable modeling for off-road tire traction analysis [19]. Novel compatible modeling between FEM and DEM for the tire traction analysis is examined in order to reduce the DEM computational cost. In the method named iFE–DEM, the soil in a soil bin is initially modeled using FEM, except for the region under or near the tire, which is modeled

using DEM. When the FEM tire model begins travelling over the DEM soil elements, the updated tire location will activate a new conversion of modeling from FEM to DEM for the path in front of the tire such that the zone of impact around the contact interface between the tire and the soil can be continuously analyzed using DEM. The mobilized DEM elements rearward of the tire might again be converted into FEM elements.

Finally, Chapter 6 presents the conclusions of the dissertation, along with a summary of recommendations for future work.

References

- [1] Aubel, Th. 1992. FEM-Simulation der Wechselwirkung zwischen Reifen und nachgiebiger Fahrbahn. *Automobiltechnische Zeitschrift* 94: 662-667.
- [2] Asaf, Z., I. Shmulevich, and D. Rubinstein. 2006. Predicting soil-rigid wheel performance using distinct element method. *Trans. ASABE* 49(3): 607-616.
- [3] Bekker, M. G.. 1956. *Theory of land locomotion*. The University of Michigan Press, Ann Arbor.
- [4] Bekker, M. G.. 1969. *Introduction to terrain-vehicle systems*. The University of Michigan Press, Ann Arbor.
- [5] Cundall, P. A. and O. D. L. Strack. 1979. Discrete numerical model for granular assemblies. *Geotechnique* 29(1): 47-65.
- [6] Favaedi, Y., A. Pechev, M. Scharringhausen, and L. Richter. 2011. Prediction of tractive response for flexible wheels with application to planetary rovers. *Journal of Terramechanics* 48: 199-213.
- [7] Fervers, C. W. 1996. Tyre profile effects on wheel-soil interaction. *Proc. 12th Int. Conf. ISTVS, Beijing, PRC*, 203-214.
- [8] Hiroma, T. , Y. Ohta, and T. Kataoka. 1994. Analysis of the soil deformation beneath a wheel by finite element method (Part 3). *Journal of Japanese Society of Agricultural Machinery* 56(6): 3-10. (in Japanese)
- [9] Janosi, Z. and B. Hanamoto. 1961. The analytical determination of drawbar pull as a function of slip for tracked vehicles in deformable soils. In: *Proc. 1st International Conference on the Mechanics of Soil-Vehicles Systems*, Turin.
- [10] Johnson, J. B., A.V. Kulchitsky, P. Duvoy, K. Iagnemma, C. Senatore, R. E. Arvidson, and J. Moore. 2015. Discrete element method simulations of Mars Exploration Rover wheel performance. *Journal of Terramechanics* 62: 31-40.

- [11] Knuth, M. A., J. B. Johnson, M. A. Hopkins, R. J. Sullivan, and J. M. Moore. 2012. Discrete element modeling of a Mars Exploration Rover wheel in granular material. *Journal of Terramechanics* 49: 27-36.
- [12] Liu, C. H. and J. Y. Wong. 1996. Numerical simulations of tire-soil interaction based on critical state soil mechanics. *Journal of Terramechanics* 33(5): 209-221.
- [13] Lyasko, M.. 2010. Slip sinkage effect in soil-vehicle mechanics. *Journal of Terramechanics* 47: 21-31.
- [14] Matsushima, T., J. Katagiri, K. Uesugi, A. Tsuchiyama, and T. Nakano. 2009. 3D shape characterization and image-based DEM simulation of the lunar soil simulant FJS-1. *Journal of Aerospace Engineering* 22(1), 15-23.
- [15] Nakashima, H., H. Fujii, A. Oida, M. Momozu, Y. Kawase, H. Kanamori, S. Aoki, and T. Yokoyama. 2007. Parametric analysis of lugged wheel performance for lunar microrover by means of DEM. *Journal of Terramechanics* 44: 153-162.
- [16] Nakashima, H., H. Fujii, A. Oida, M. Momozu, H. Kanamori, S. Aoki, T. Yokoyama, H. Shimizu, J. Miyasaka, and K. Ohdoi. 2010. Discrete element method analysis of single-wheel performance for a small lunar rover on sloped terrain. *Journal of Terramechanics* 47: 307-321.
- [17] Nishiyama, K., H. Nakashima, T. Yoshida, T. Ono, H. Shimizu, J. Miyasaka, and K. Ohdoi. 2016. 2D FE–DEM analysis of tractive performance of an elastic wheel for planetary rovers. *Journal of Terramechanics* 64: 23-35.
- [18] Nishiyama, K., H. Nakashima, H. Shimizu, J. Miyasaka, and K. Ohdoi. 2017. 2D FE–DEM analysis of contact stress and tractive performance of a tire driven on dry sand. *Journal of Terramechanics* 74: 25-33.
- [19] Nishiyama, K., H. Nakashima, T. Yoshida, H. Shimizu, J. Miyasaka, and K. Ohdoi. 2018. FE–DEM with interchangeable modeling for off-road tire traction analysis. *Journal of Terramechanics* 78: 15-25.
- [20] Oida, A., A. Satoh, H. Itoh, and K. Triratanasirichai. 1991. Three-dimensional stress distributions on a tire-sand contact surface. *Journal of Terramechanics* 28: 319-330.
- [21] Oida, A., S. Ohkubo, and H. Schwanghart. 1999. Effect of tire lug cross section on tire performance simulated by distinct element method. Proc. 13th Int. Conf. ISTVS, Munich, Germany, 345-352.
- [22] Ozaki, S., K. Hinata, C. Senatore, and K. Iagnemma. 2015. Finite element analysis of periodic ripple formation under rigid wheels. *Journal of Terramechanics* 61: 11-22.

- [23] Pruiksma, J. P., J. A. M. Teunissen, G. A. M. Kruse, and M. van Winnendael. 2011. Tractive Performance Modelling of the ExoMars Rover Wheel Design on Loosely Packed Soil Using the Coupled Eulerian Lagrangian Finite Element Technique. <http://robotics.estec.esa.int/ASTRA/Astra2011/Presentations/Session%202> (accessed on 23 Dec, 2018)
- [24] Senatore, C. and C. Sandu. 2011. Off-road tire modeling and the multi-pass effect for vehicle. *Journal of Terramechanics* 48: 265-276.
- [25] Shoop, S.. 2001. Finite element modeling of tire-terrain Interaction. Technical Report, ERDC/CR- REL TR-01-16.
- [26] Smith, W. and H. Peng. 2013. Modeling of wheel-soil interaction over rough terrain using the discrete element method. *Journal of Terramechanics* 50: 277-287.
- [27] Ueno, M., K. Hashiguchi, Y. Nose, F. Koyama, K. Uchiyama, and H. Izumi. 1990. Analysis of soil-wheel interaction by elastoplastic finite element method. In: Proc. 10th Int. Conf. of ISTVS, Kobe, 253-264.
- [28] Wong, J. Y. and A. R. Reece. 1967. Prediction of rigid wheel performance based on the analysis of soil-wheel stresses—Part 1. Performance of driven rigid wheels—. *Journal of Terramechanics* 4: 81-98.
- [29] Wong, J. Y.. 1993. *Theory of Ground Vehicle*, Second Edition. A Wiley-Interscience Publication John Wiley & Sons, Inc., NY.
- [30] Xia, K.. 2011. Finite element modeling of tire/terrain interaction: Application to predicting soil compaction and tire mobility. *Journal of Terramechanics* 48: 113-123.
- [31] Yong, R. N. and E. A. Fattah. 1976. Prediction of wheel-soil interaction and performance using the Finite Element Method. *Journal of Terramechanics* 13(4): 227-240.
- [32] Yong, R. N., E. A. Fattah, and P. Boonsinsuk. 1978. Analysis and prediction of tyre-soil interaction and performance using finite elements. *Journal of Terramechanics* 15(1): 43-63.
- [33] Zhong, Z. H. 1993. *Finite element procedures for contact-impact problems*. Oxford Univ. Press, Oxford.

Chapter 2

Overview of FE–DEM

2.1 Introduction

The idea of FE–DEM is not new, and there are many publications in applied mechanics and engineering problems utilizing this method. Textbooks on FE–DEM can also be found [4, 5].

Pan and Reed [10] applied the coupled DE–FE method to rock mechanics problems. Flow problems in silo were also solved using the DE–FE method [2]. Horner et al. [1] demonstrated the capability of the precise and detailed application of massive-scale DEM and FEM to some problems in terramechanics. Furthermore, an algorithm and implementation of 2D FE–DEM for tire sinkage into soil were reported [6]. Subsequently, 2D FE–DEM was applied to analyze the tractive performance of smooth automotive tires, for which deformation was negligible (i.e., rigid contact mode) [7]. Moreover, the study results reported in [8] indicated that the 2D FE–DEM analysis of the tractive performance of tires with lug-patterned treads can achieve sufficient accuracy as compared to that of the study reported in [12], as shown in Figure 2-1 [8].

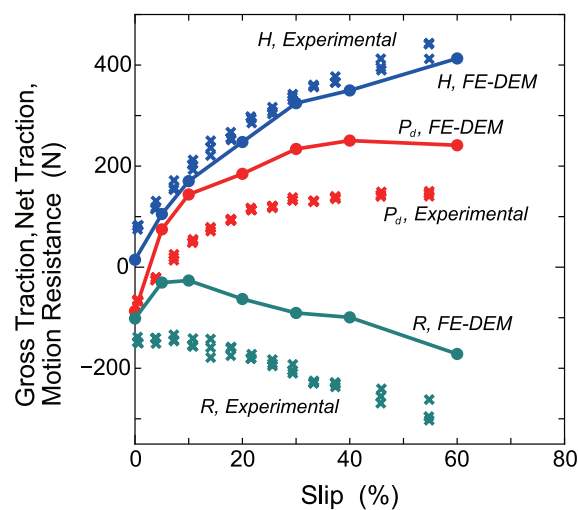


Figure 2-1: Result of the tractive performance of a tire with lug-patterned treads [8].

In FE-DEM analysis, the net traction is calculated from the difference of the gross traction and motion resistance. Thus, the source of deviation in the net traction is the deviated result of the motion resistance. An attempt to analyze the tractive performance of an elastic iron wheel using FE-DEM was reported in [9]. The results of this analysis are illustrated in Figure 2-2, which demonstrates that the exhibited net traction deviates from the experimental result, whereas the motion resistance becomes smaller in magnitude as the wheel slip increases.

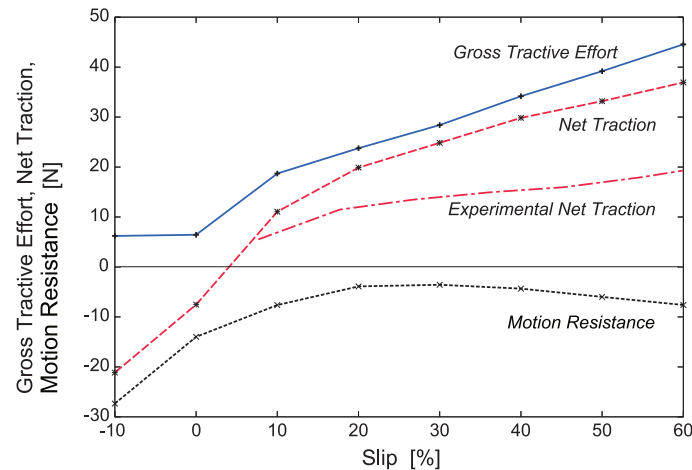


Figure 2-2: Result of the tractive performance of an elastic iron wheel [9].

Based on the observations in [8, 9], it is clear that further research on developing a more accurate FE-DEM algorithm for tractive performance analysis is required.

Recently, a wheel performance analysis using 3D FE-DEM was attempted using a desktop PC, achieving a computational time of 96 h; however, no precise information on the motion resistance and gross tractive effort was reported [13]. Note that the wheel was assumed to be rigid and the diameter of the DEM elements was as large as 14 mm [14]. Furthermore, the tractive performance of an off-road tire on soil was analyzed using a 3D DEM-FEM coupling method [3]; however, the soil bin model was too shallow for the interaction of the off-road tire in this study. Reportedly, a comparable numerical result was obtainable, although the case of 5% slip was shown representatively as a result of applying 3D FE-DEM in comparison with the experimental results from earlier studies [12]. From these results, using 3D FE-DEM for estimating the tractive performance of off-road tires is understood to be premature under the current developmental state of computer technologies.

The 2D FE-DEM analysis is summarized below on the basis of the previous reports of our research group at the Laboratory of Agricultural Systems Engineering, Kyoto University [7, 8].

2.2 Formulation of FE-DEM

The tire and subsurface soil are modeled as elastic bodies in FEM. DEM is applied in modeling the upper soil layer, where the shear and large deformation of soil under the action of a tire or tire treads

would be expected.

We must solve two types of equations of motion, one for translation (for both FEM and DEM) and the other for rotation (for DEM), which are represented using vector notation as follows:

$$\mathbf{F}_c + \mathbf{F}_b = m \frac{d^2 \mathbf{u}}{dt^2} \quad (\text{for FEM, DEM}) \quad (2.1)$$

$$\mathbf{N}_c = I \frac{d^2 \boldsymbol{\theta}}{dt^2} \quad (\text{for DEM}), \quad (2.2)$$

where \mathbf{F}_c denotes the contact reaction, \mathbf{F}_b denotes the volumetric force, m denotes the mass, \mathbf{u} denotes the displacement, \mathbf{N}_c denotes the moment by \mathbf{F}_c , I denotes the moment of inertia, and $\boldsymbol{\theta}$ denotes the rotational displacement. Naturally, there are x - and y -components in Eq. (2.1) and one component in Eq. (2.2) in the case of a 2D FE–DEM problem. Explicit time integration is applied to solve the above equations.

2.3 Numerical integration method

The equations of motion, that is, Eqs. (2.1) and (2.2), are discretized in the time domain to execute time integration numerically.

2.3.1 FEM

The dynamic explicit method is used for FEM because the considered problem can be classified as a large-scale dynamic analysis. For a detailed expression of the FEM formulation, Eq. (2.1) can be rewritten as follows:

$$m\ddot{\mathbf{u}} + c\dot{\mathbf{u}} + \mathbf{f} = \mathbf{p}, \quad (2.3)$$

where m is the diagonal component vector extracted from the lumped mass matrix, c is the damping vector, \mathbf{f} is the internal force vector, and \mathbf{p} is the external force vector.

The internal force vector (\mathbf{f}) can be calculated as

$$\mathbf{f} = \mathbf{K}\mathbf{u}, \quad (2.4)$$

where \mathbf{K} denotes the total stiffness matrix, which can be obtained by summation of the element stiffness matrixs (\mathbf{K}^e) calculated as

$$\mathbf{K}^e = \int_S \mathbf{B}^T \mathbf{D} \mathbf{B} t dS, \quad (2.5)$$

where \mathbf{B} and \mathbf{D} are the B-matrix and D-matrix, respectively, which express relationships within FEM meshes between displacement and strain for the B-matrix and between strain and stress for the D-matrix; t denotes the element's thickness. The D-matrix for a tire is assumed to represent the plane stress condition because the tire is not constrained in the tire width direction. In contrast, the

D-matrix for soil is assumed to represent the plane strain condition because the soil is confined by the wall of the soil bin.

Difference approximations can be expressed according to the central difference method as follows:

$$\dot{\mathbf{u}}^t = \frac{\mathbf{u}^{t+\Delta t} - \mathbf{u}^{t-\Delta t}}{2\Delta t}, \quad (2.6)$$

$$\ddot{\mathbf{u}}^t = \frac{\mathbf{u}^{t+\Delta t} - 2\mathbf{u}^t + \mathbf{u}^{t-\Delta t}}{\Delta t^2}, \quad (2.7)$$

where t denotes the current time and Δt signifies the time step.

By substituting Eqs. (2.6) and (2.7) into Eq. (2.3), the nodal displacement at the next time step can be obtained as follows:

$$\mathbf{u}^{t+\Delta t} = \frac{\mathbf{p} - \mathbf{f} + \mathbf{m} \frac{1}{\Delta t^2} (2\mathbf{u}^t - \mathbf{u}^{t-\Delta t}) + \mathbf{c} \frac{1}{2\Delta t} \mathbf{u}^{t-\Delta t}}{\frac{1}{\Delta t^2} \mathbf{m} + \frac{1}{2\Delta t} \mathbf{c}}. \quad (2.8)$$

2.3.2 DEM

For DEM time integration, a modified Euler method is used in this study to balance the computational cost and error rate. Let the acceleration be \mathbf{a} , the velocity be \mathbf{v} , and the displacement be \mathbf{u} . Then, the discretized time integration for translation can be represented as

$$\mathbf{v}(t + \Delta t) = \mathbf{v}(t) + 0.5 (\mathbf{a}(t) + \mathbf{a}(t + \Delta t)) \Delta t \quad (2.9)$$

$$\mathbf{u}(t + \Delta t) = \mathbf{u}(t) + 0.5 (\mathbf{v}(t) + \mathbf{v}(t + \Delta t)) \Delta t. \quad (2.10)$$

Similarly, let the angular acceleration be $\boldsymbol{\alpha}$, the angular velocity be $\boldsymbol{\omega}$ and the angular displacement be $\boldsymbol{\theta}$. Then, the discretized time integration for rotation can be expressed as

$$\boldsymbol{\omega}(t + \Delta t) = \boldsymbol{\omega}(t) + 0.5 (\boldsymbol{\alpha}(t) + \boldsymbol{\alpha}(t + \Delta t)) \Delta t \quad (2.11)$$

$$\boldsymbol{\theta}(t + \Delta t) = \boldsymbol{\theta}(t) + 0.5 (\boldsymbol{\omega}(t) + \boldsymbol{\omega}(t + \Delta t)) \Delta t. \quad (2.12)$$

2.4 Tractive performance analysis of a tire using FE-DEM

Figure 2-3 illustrates the horizontal contact reaction for the gross tractive effort and running resistance of a tire in FE-DEM [8]. The tire is assumed to travel to the right with some positive tire slip. Consequently, we can calculate the gross tractive effort, or gross traction, H , of a tire as follows:

$$H = \sum f_x^+, \quad (2.13)$$

whereas the motion resistance R (< 0) can be obtained as follows:

$$R = \sum f_x^-, \quad (2.14)$$

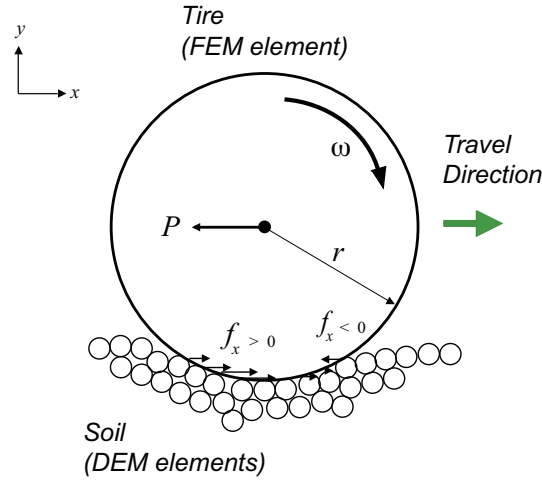


Figure 2-3: Horizontal contact reaction at the soil-tire interface [8].

where f_x^+ and f_x^- are the positive and negative components of contact reaction at the tire-soil interface acting on the contact nodes of tire FEs with respect to the global coordinate system (Figure 2-3).

Based on Eqs. (2.13) and (2.14), a well-known relationship for net traction P_d can be calculated as follows:

$$P_d = H - |R|, \quad (2.15)$$

which becomes equal to the drawbar pull P (see Figure 2-3).

The slip i of a tire can be expressed as

$$i = \frac{V_w - V}{V_w} = \left(1 - \frac{V}{r\omega}\right), \quad (2.16)$$

where V denotes the translation speed of the tire center, V_w denotes the circumferential velocity of the tire, r denotes the rolling radius of a free-rolling tire, and ω denotes its angular velocity; note that $V_w = r\omega$. The constant angular velocity (ω) and constant translational velocity (V) of a tire are the inputs in our FE–DEM to compare the experimental result [11, 12]. The tractive performance is analyzed on the basis of the constant slip value of i defined by Eq. (2.16).

2.5 Contact reaction

Figure 2-4 shows a typical linear contact model in DEM comprising a spring and a damper placed in parallel to calculate contact reactions in the normal and tangential directions.

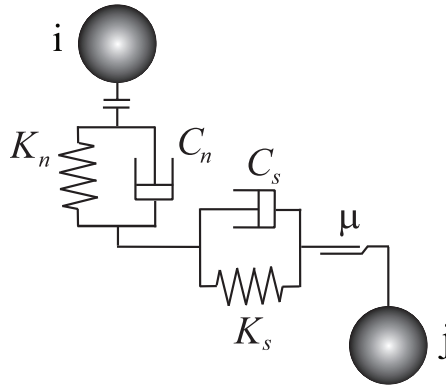


Figure 2-4: Linear contact model for DEM [7].

Each component of the reaction in the j -direction (i.e., $j = n$ for the normal direction or $j = s$ for the tangential direction) can be expressed as

$$F_j = K_j \Delta u_j + C_j \Delta \dot{u}_j \quad (j = n, s), \tag{2.17}$$

where F_j is the contact reaction, Δu_j is the relative displacement of the contacting elements, K_j is the spring constant, C_j is the damping coefficient, and $\Delta \dot{u}_j$ is the relative velocity of the contacting elements. For the tangential reaction, Coulomb friction may also be considered, such that $F_s = \mu F_n$ if $F_s > \mu F_n$ and $F_s = F_s^*$ if $F_s < \mu F_n$ with a friction coefficient of μ and F_s^* denoting an updated tangential reaction.

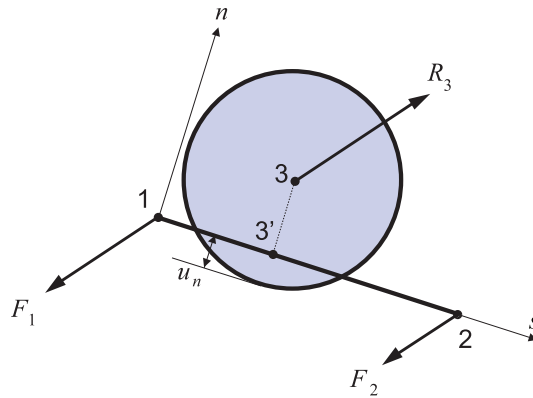


Figure 2-5: Contact model of the interface in FE-DEM [7].

Figure 2-5 depicts a contact model at the FE-DEM interface, where we focus on line segment 1-2 of an FE for the 2D case to distribute the contact reaction linearly into nodal reactions F_1 and F_2 using contact force R_3 in DEM. As illustrated in the figure, the contact between the FE mesh and the DE can be treated, in most parts in the 2D case, as the contact between DEs with a slight modification of the redistribution of the contact reaction using a shape function on the supporting nodes of a contacting line segment of the FE mesh.

Figure 2-6 shows a schematic diagram of the rolling resistance model, where element i is assumed to be in contact with element j .

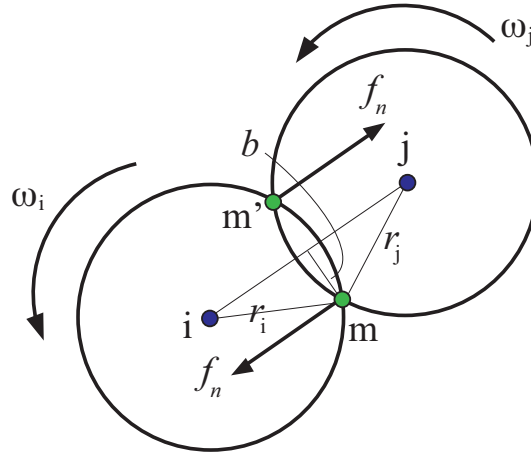


Figure 2-6: Rolling resistance moment

In order to prevent circular DEM elements from rotating excessively as a result of a poor representation of the interlock effect within the soil granular structure, a rolling resistance moment is introduced in this study [16]. The rolling resistance moment N_r can be calculated in the direction opposite to the angular velocity ω as follows:

$$\begin{cases} N_r = -\alpha b f_n & (\omega > 0) \\ N_r = \alpha b f_n & (\omega < 0), \end{cases} \quad (2.18)$$

where b denotes the length from the crossing point of elements i and j (point m in Figure 2-6) to the contact center line, f_n denotes the spring reaction force in the normal direction, and α is the influence coefficient.

2.6 Program flow

Figure 2-7 shows the schematic flow of the combined FE–DEM for the soil–tire interaction study presented in [7].

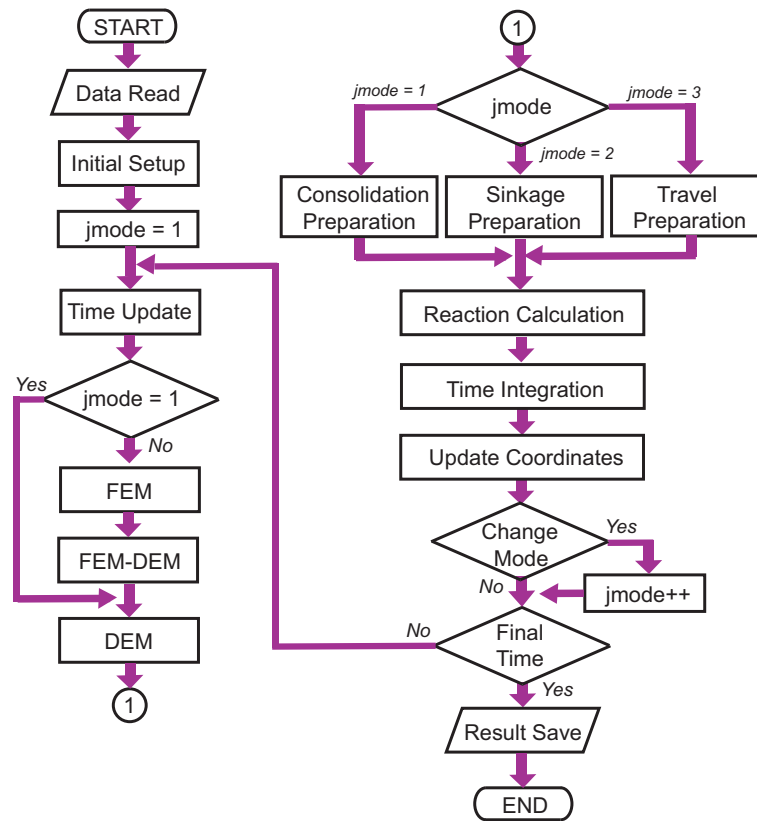


Figure 2-7: Schematic flow of the proposed FE-DEM program [7].

The simulation strategy comprises the following three modes: (i) soil consolidation by the weight of DEs at the surface soil layer, (ii) free sinkage of tire FEs into the soil surface until the vertical contact reaction of the tire reaches the vertical load of the tire, and (iii) tire travel mode with prescribed angular and translational velocities. In the program, these three modes are switched on sequentially on the basis of the prescribed time step for each mode.

References

- [1] Horner, D. A., J. F. Peters, and A. Carrillo. 2001. Large scale discrete element modeling of vehicle-soil interaction. *Journal of Engineering Mechanics* 127(10): 1027-1032.
- [2] Lu, Z., S.C. Negi and J.C. Jofreit. 1997. A numerical model for flow of granular materials in silos, Part 1: Model development. *Journal of Agricultural Engineering Research* 68: 223-229.
- [3] Michael, M., F. Vogel, and B. Peters. 2015. DEM-FEM coupling simulations of the interactions between a tire tread and granular terrain. *Comput. Methods Appl. Mech. Engng* 289: 227-248.
- [4] Mohammadi, S.. 2003. *Discontinuum mechanics using finite and discrete elements*. WITpress, Southampton.

- [5] Munjiza, A.. 2004. The combined finite–discrete element method. John Wiley & Sons Ltd, Chichester.
- [6] Nakashima, H. and A. Oida. 2004. Algorithm and implementation of soil-tire contact analysis code based on dynamic FE-DE method. *Journal of Terramechanics* 41: 127-137.
- [7] Nakashima, H. and Y. Takatsu. 2008. Analysis of tire tractive performance on deformable terrain by finite element–discrete element method. *Journal of Computer Science and Technology* 2(4), 423-434.
- [8] Nakashima, H., Y. Takatsu, H. Shinone, H. Matsukawa, and T. Kasetani. 2009. FE–DEM analysis of the effect of tread pattern on the tractive performance of tires operating on sand. *Journal of Mechanical Systems for Transportation and Logistics* 2 (1): 55-65.
- [9] Ono, T., H. Nakashima, H. Shimizu, J. Miyasaka, and K. Ohdoi. 2010. Analysis of elastic wheel performance for off-road mobile robots using FE–DEM. In: *Proc. the Third IFAC International Conference Agricontrol*, 61-66. (<http://dx.doi.org/10.3182/20101206-3-JP-3009.00010>)
- [10] Pan, X. D. and M. B. Reed. 1991. A coupled distinct element-finite element method for large deformation analysis of rock masses. *Int. J. Rock Mech. Min. Sci. & Geomech. Abstr.*, 28(1): 93-99.
- [11] Shinone, H.. 2009. Improvement of an indoor traction measurement system based on a forced slip mechanism. Unpublished Master of Agricultural Sciences Thesis, Division of Environmental Science & Technology, Graduate School of Agriculture, Kyoto University. (in Japanese)
- [12] Shinone, H., H. Nakashima, Y. Takatsu, T. Kasetani, H. Matsukawa, H. Shimizu, J. Miyasaka, and K. Ohdoi. 2010. Experimental analysis of tread pattern effects on tire tractive performance on sand using an indoor traction measurement system with forced-slip mechanism. *Engineering in Agriculture, Environment and Food* 3(2): 61-66.
- [13] Zhao, C. and M. Zang. 2014. Analysis of rigid tire traction performance on a sandy soil by 3D finite element–discrete element method. *Journal of Terramechanics* 55: 29-37.
- [14] Zhao, C. and M. Zang. 2017. Application of the FEM/DEM and alternately moving road method to the simulation of tire-sand interactions. *Journal of Terramechanics* 72: 27-38.
- [15] Zhong, Z. H. 1993. Finite element procedures for contact-impact problems. Oxford Univ. Press, Oxford.
- [16] Zhou, Y. C., B. D. Wright, R. Y. Yang, B. H. Xu, and A. B. Yu. 1999. Rolling friction in the dynamic simulation of sandpile formation. *Physica A* 269: 536-553.

Chapter 3

Tractive performance of an elastic wheel for planetary rovers

3.1 Introduction

Recently, unmanned and manned missions to the Moon and Mars have been planned in various countries. For a Japanese unmanned mission to the Moon now being planned (SELENE-2), a small autonomous rover will be used over a slope of a crater covered by regoliths. Because of its ease in increasing contact area, it is believed that flexible or elastic metal wheels might be useful for running devices over the soft terrain with fine regolith [13]. Moreover, the European Space Agency (ESA) is preparing for an ExoMars mission to Mars in the near future, incorporating a six-wheeled robotic rover with flexible wheels [1].

This study was undertaken to extend the applicability of previously developed 2D FE–DEM code for elastic deformable wheels, as seen in recent extraterrestrial rovers reported above. A new algorithm aimed at precise simulation of a forced-slip condition of experimental traction measurement for an elastic wheel is introduced in this study. The accuracy of analysis will be compared with experimentally obtained results on the tractive performance for prototype wheels of ESA Martian rovers [8, 9].

3.2 FE-DEM analysis of wheel performance

3.2.1 Updated traction analysis

In forced-slip experiments assessing the tractive performance of tires, the drawbar pull was detected as the backward load on a tire, whereas the wheel torque was observed for a given slip condition, where the angular velocity of the tire was prescribed with the varied translational velocity of tire depending on the slip [10]. To realize similar conditions for numerical analyses, a PID-controller

model of automatic control theory is applied to ascertain loading conditions of drawbar pull P and wheel torque T .

Regarding the drawbar pull P , the following relation is assumed from the PID-controller model as

$$P = K_p^p e_x(t) + K_i^p \int_0^t e_x(t) dt + K_d^p \frac{de_x(t)}{dt} \quad (3.1)$$

where K_p^p , K_i^p , K_d^p respectively represent coefficients for proportional, integral, and derivative terms in the PID model, and $e_x(t)$ are the positions of the wheel at time t . By introducing a time step Δt into the terms in the right-hand side of Eq. (3.1) and by modifying integral symbols as summation over time from the beginning of wheel rotation and differential symbol as division, one can rewrite the relation of Eq. (3.1) as shown below.

$$P = K_p^p e_x(t) + K_i^p \sum_t e_x(t) \Delta t + K_d^p \frac{e_x(t) - e_x(t - \Delta t)}{\Delta t} \quad (3.2)$$

A block diagram for controlling the horizontal position of wheel by drawbar pull P using PID system in the updated wheel traction analysis is depicted in Figure 3-1.

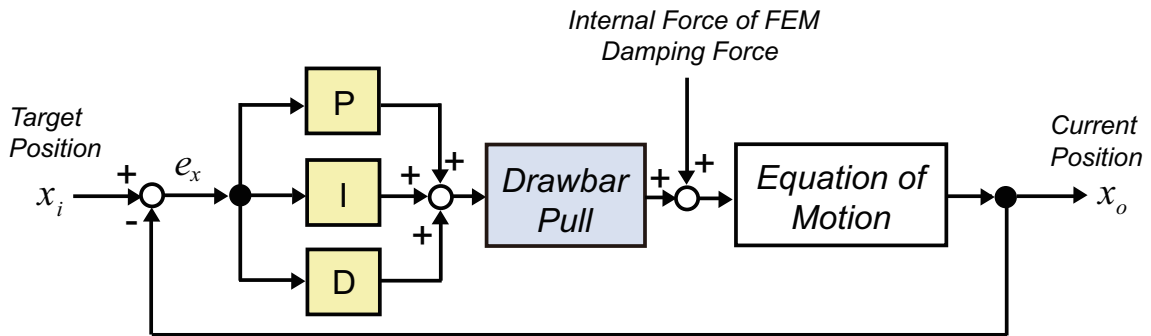


Figure 3-1: Schematic block diagram using a PID-controller model of drawbar pull with respect to a node at the rotation center of the wheel.

A numerical procedure using the drawbar pull P within the time loop for solving the equation of motion for horizontal translation is summarized as follows.

- 1) Calculation of target position using prescribed translational velocity V .
- 2) Calculation of drawbar pull using difference of wheel position via Eq. (3.2).
- 3) Calculation of internal force of FEM and damping force.
- 4) Numerical integration of the equation of motion.
- 5) Update of current position.

Since the wheel travels during the stage of traction analysis, the target position is updated based on the constant translational velocity V in the time-integration loop, which can be expressed as $\sum_{i=0}^{T_n} V \Delta t$ at the current time step T_n of the simulation. It is noteworthy that the difference or error of wheel position $e_x(t)$ at time t is calculated using $e_x(t) = x_i(t) - x_o(t)$, where $x_i(t)$ is the target position and $x_o(t)$ is the current position at time t , as in Figure 3-2 because the drawbar pulls P directly backward against the direction of wheel travel.

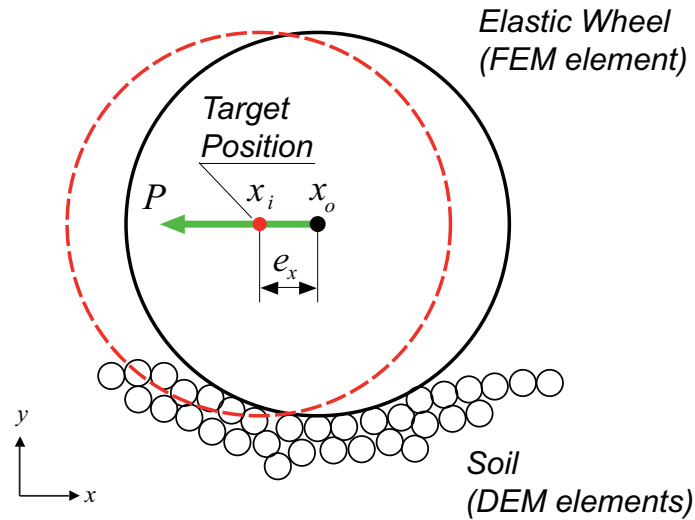


Figure 3-2: Drawbar pull and target horizontal position.

It is noteworthy that some ideas of proportional control of horizontal velocity exist already in the literature [11], although no detailed explanation of it is given.

Similarly, we can produce a computational expression for wheel torque T by a PID-controller model such that

$$T = K_p^t e_\theta(t) + K_i^t \sum_t e_\theta(t) \Delta t + K_d^t \frac{e_\theta(t) - e_\theta(t - \Delta t)}{\Delta t} \quad (3.3)$$

where K_p^t , K_i^t , and K_d^t are coefficients for the proportional, integral, and derivative terms in the PID model for wheel torque, $e_\theta(t)$ denotes the difference of the rotation angle of the wheel at time t , and Δt is the time step.

A block diagram for controlling the angular position of the wheel by wheel torque T using a PID system is the same as in Figure 3-1, by replacing position x to the rotation angle θ and drawbar pull P to wheel torque T .

A numerical procedure for wheel rotation using wheel torque T for solving the equation of motion is then summarized as presented below.

- i) Calculation of the target rotation angle using angular velocity ω .
- ii) Calculation of the wheel torque using the difference of angle via Eq. (3.3).
- iii) Calculation of the distribution of force for each surface nodes of wheel rim.

- iv) Calculation of the internal force of FEM and damping force.
- v) Numerical integration of the equation of motion.
- vi) Update of the current rotation angle.

For calculation of rotation angles in i) and vi) reported above, the angle for each node at the surface of the wheel rim is updated.

The difference or error of wheel angular position $e_\theta(t)$ at time t is calculated by $e_\theta(t) = \theta_i(t) - \theta_o(t)$ as in Figure 3-3 because the wheel torque T is applied clockwise, which is the same direction as the angular velocity ω , where $\theta_i(t)$ is the target angular position and $\theta_o(t)$ is the current angular position at time t .

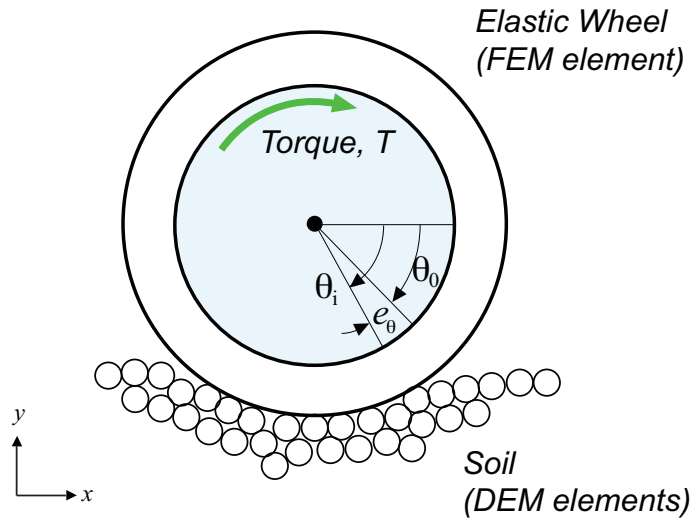


Figure 3-3: Wheel torque and target rotation angle.

It is noteworthy that the current angle of rotation $\theta_o(t)$ is calculated as an average of all nodes at the surface of the wheel rim modeled by FE, such that

$$\theta_o(t) = \frac{\sum_{j=1}^N \theta_o^j(t)}{N}, \quad (3.4)$$

where $\theta_o^j(t)$ stands for the angle at a node j on the surface of the wheel rim at time t , and N represents the total number of finite element nodes on the wheel rim surface.

Using the drawbar pull P from Eq. (3.2) and the wheel torque T from Eq. (3.3), we can calculate the traction performance of an elastic wheel as shown below.

$$\text{Gross tractive effort: } H = T/r_e \quad (3.5)$$

$$\text{Net traction: } P_d = -P \quad (3.6)$$

$$\text{Motion resistance: } R = H - |P| \quad (3.7)$$

Therein, r_e represents the effective rolling radius of wheel obtained as the minimum radius of wheel in the analysis. The contact surface of a wheel with soil is assumed to be horizontal in the derivation of gross tractive effort H .

The slip i of a wheel is expressed as

$$i = \left(1 - \frac{V}{r_e \omega}\right) \times 100 \quad [\%] \quad (3.8)$$

where V signifies the translational velocity of a wheel and ω denotes the angular velocity of the wheel. It is noteworthy that either V or ω should be controlled against the prescribed slip of wheel i in the forced-slip formulation of FE-DEM.

3.2.2 Structure of the wheel model and parameters

Experimental data collected at the German Space Center (DLR), Bremen, Germany, were used to investigate the accuracy of the solution using 2D FE-DEM. Elastic wheels in experiments consist of flexible wheels of two types, B3 and B6 shown in Figure 3-4, as developed as a prototype for ExoMars rover by ESA expected to be deployed around 2018 [8, 9]. These two wheels had the same geometrical dimensions, but the total number and structure of spokes differed such that the radial stiffness can be varied [9].



Figure 3-4: Elastic wheels in experiments (left, B3; right, B6). [9]

Figure 3-5 portraying a computational model of the elastic wheel expressed by FEM. The wheel model consists of the following four parts: wheel rim (WR), intermediate layer (WI), surface layer (WS), and wheel lugs (WL). Intermediate layer rigidity can control the elastic behavior of the wheel [7, 12, 4]. Over the surface of WS, characteristic U-shaped lugs were distributed by the combination of quadrilateral finite elements, as shown in a close-up view in Figure 3-5, although, in practice, the small soil volume between U-shaped double grouser might not contribute meaningfully to thrust generation [9]. It is noteworthy that a limiter of deflection observable as the inner circle plate at the rim part of both wheels in Figure 3-4 is not implemented in the current wheel model used for FE-DEM analysis.

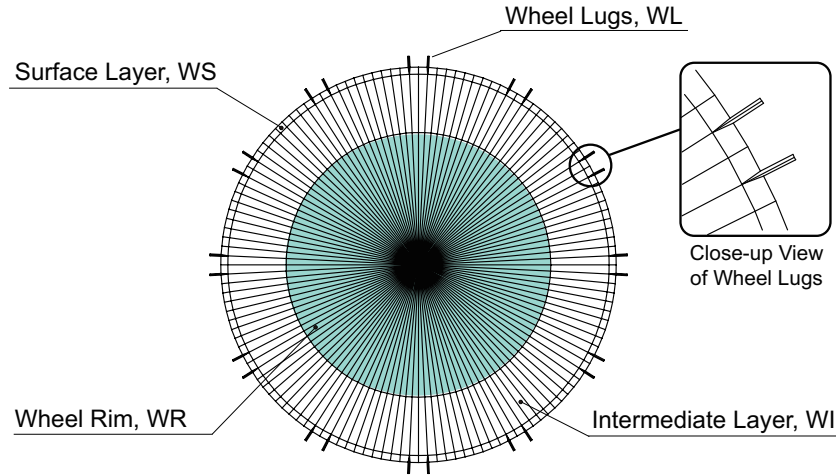


Figure 3-5: Model elastic wheel.

Elastic wheels specifications are presented in Table 3-1. Numerical parameters for FE–DEM are listed in Table 3-2, 3-3 and 3-4.

The total number of finite elements for wheel model is 493, with the total number of nodes of 444 for wheel models [7]. Young’s Moduli of finite elements at the wheel rim (WR) were decided by trial and error, considering the stability of computation, although Poisson’s ratios of 0.3 were assumed for WR. Young’s Moduli and Poisson’s Ratios for wheel surface layer (WS) and wheel lugs (WL) in Table 3-3 were chosen arbitrarily by consideration of our previous experiences of FE–DEM [7, 12, 4].

Radial stiffness K_c of an elastic wheel can be expressed as

$$K_c = \frac{W}{\delta}, \quad (3.9)$$

where W stands for the wheel contact load, and where δ signifies the elastic wheel deflection on a rigid horizontal surface. Actually, a B3 wheel, with radial stiffness of $K_c = 14.3$ N/mm, is easier to deform than a B6 wheel with $K_c = 53.0$ N/mm [9]. Using preliminary computations, we adjusted the Young’s modulus of intermediate layer (WI) of each wheel so that the numerical radial stiffness became similar to the measured stiffness stated above. Consequently, the radial stiffness by FE–DEM was found as $K_c = 15.9$ N/mm (B3 wheel) and 53.2 N/mm (B6 wheel).

Elemental densities for WR and WL are increased so that the time step Δt can be increased under the limitations of the Courant condition in explicit dynamic FEM [14]. Rolling resistance moment M_r is also introduced into the current analysis for soil DEM to prevent the excessive rotation of circular soil elements, such that $M_r = -bf_n$, where b denotes the tangential contact length of soil elements under contact, and f_n stands for the normal contact reaction.

In the experiment, the slip was defined by the relative difference of velocities between the constant translation V and variable rotation of wheel ω as in Eq. (3.8) [9], where larger ω should be

input for the larger wheel slip. In FE–DEM, the translational velocity is fixed to $V = 100$ mm/s, which is larger than the experimental velocity of 10 mm/s considering the computational cost in the analysis. It is noteworthy that the result of FE–DEM with $V = 10$ mm/s exhibits no significant difference in the result of traction performance with $V = 100$ mm/s. The slip of wheel was set as 0, 10, \dots , 70% with an increment of 10%, by varying the angular velocity of wheel ω . The wheel load was varied selectively in the range of 50 N and 170 N in terms of the corresponding experimental conditions, as in Table 3-1.

The elastic parameters for the intermediate layer (WI) of each wheel are presented in Table 3-2. Dry sand is the target soil. A linear contact model consisting of a spring and damper connected in parallel is used for discrete elements of soil. Spring constants for discrete elements were chosen by consideration of our previous experiences with soil–wheel contact studies [12]. The total number of soil elements for DEM is 19,468. The radii of soil elements are set as 2.0, 2.5 and 3.0 mm, with the ratio of number as 3:2:1.

The time step was chosen as 1.0×10^{-5} s. By this time step, the elapsed time of current FE–DEM for one slip condition was 45,400 s (12.61 hr) at maximum, using a PC-based Linux computer. It is noteworthy that the rolling resistance moment is applied for DEM contacts and FE–DEM contacts.

In Table 3-3, the friction coefficient between soil elements and wheel WS was chosen using trial-and-error preliminary analysis. For the initial preparation of soil elements, the friction coefficients between soil elements and between soil element and wall element were set to 0.0 to make soil elements settle easily into the model soil bin.

Table 3-1: Specifications of elastic wheels. [9]

Maximum diameter of wheel [mm]	316
Diameter of wheel rim [mm]	180
Width of wheel [mm]	100
Wheel contact load, W [N]	50, 70, 100, 130, 170
Total number of lugs [-]	24 (12×2)
Lug height [mm]	8
Radial stiffness, K_c [N/mm]	14.3 (B3), 53.0 (B6)
Translational velocity, V [mm/s]	10.0 (100.0 \dagger)
Travel distance	two wheel rotations (800 mm \dagger)
Angular velocity, ω [rad/s]	<i>varied</i>
	\dagger for FE–DEM only

Table 3-2: Parameters of FE–DEM (1).

	Wheel				Soil
	WR	WI	WS	WL	
Radius of discrete elements [mm]	–	–	–	–	2,2.5,3 (3:2:1)
Total number of discrete elements	–	–	–	–	19468
Young's Modulus [MPa] (B3)	200	0.05	4	4	–
Young's Modulus [MPa] (B6)	200	0.3	4	4	–
Poisson's Ratio (B3)	0.3	0.3	0.49	0.49	–
Poisson's Ratio (B6)	0.3	0.3	0.49	0.49	–
Elemental density [kg/m ³]	3000	1000	1000	5000	2600

Table 3-3: Parameters of FE–DEM (2).

	SE*-WS(WL)	SE*-SE*	SE*-DW†
Normal spring const. [kN/m]	100	100	100
Tangential spring const. [kN/m]	25	25	25
Friction coeff. [-]	0.1	0.6 (0.0‡)	0.4 (0.0‡)

(NB) *SE, soil elements; †DW, wall discrete elements

‡Friction coefficient of 0.0 applies to consolidation stage only.

Table 3-4 presents the PID coefficients used in Eqs. (3.2) and (3.3). They were chosen based on several preliminary analyses in terms of the stability in force, travel distance, and rotation angle of wheel against the elapsed time of wheel travel without an excess increase in differences e_x and e_θ . Presumably the coefficients listed in the table can be applied commonly to the two elastic wheel models that were investigated. Moreover, it is noteworthy that combinations of those coefficients in the table have not been fully investigated. Examination of these combinations is beyond the scope of this study.

Table 3-4: Parameters of FE–DEM (3).

	Coefficient	Value
P	K_p^p [N/m]	1.0×10^4
	K_i^p [N/(m·s)]	1.0×10^4
	K_d^p [Ns/m]	1.0×10^4
T	K_p^t [Nm/rad]	1.0×10^3
	K_i^t [Nm/(rad·s)]	1.0×10^3
	K_d^t [Nms/rad]	1.0×10^3

The procedure of FE–DEM analysis for wheel traction comprises three steps [5, 12]. First, the soil elements are generated and filled into the soil bin. Then, the consolidation of soil elements by their own weight is applied for 1 s. Secondly, the free sinkage of wheel finite elements by application of wheel load at the node of rotation center of wheel is analyzed for 2 s so that the reaction from soil models can be stabilized sufficiently. Lastly, the analysis of wheel travel starts with acceleration of 1 s until the velocity for the prescribed slip condition is achieved. Then, the wheel continues to travel to a specified travel distance of 80 cm.

3.3 Results and discussion

3.3.1 Results of numerical analysis

The result of traction analysis by FE–DEM was obtained by averaging the result for the latter period of horizontal wheel travel with constant translational velocity. The interval of travel distance for averaging was 40–80 cm for $i \leq 60\%$ and 60–80 cm for $i = 70\%$ because of the stable results of analysis.

B3 Wheel

Figure 3-6 presents an example of wheel and soil deformation at the end of travel for $i = 20\%$ with $W = 170$ N. The shape of contact interface between the wheel and soil shows not only small sinkage but also noticeable deformation of the wheel surface layer, which is caused by the reduced rigidity of the intermediate layer of the wheel. It was confirmed in many studies reported in the literature that the shape of the contact interface resembles the shape of moving tire deformation [3].

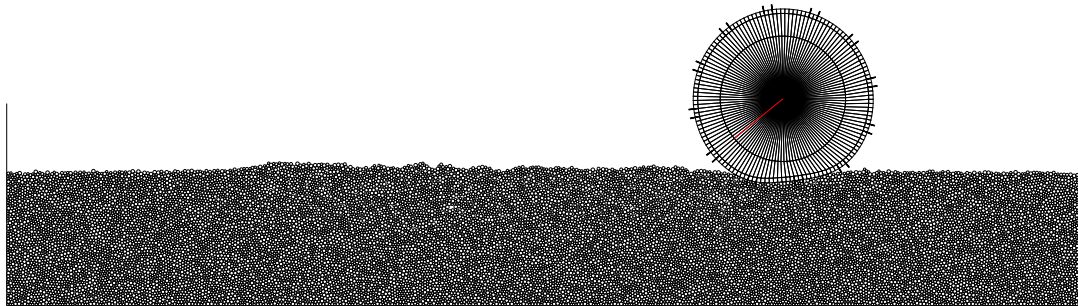


Figure 3-6: Example of wheel and soil deformation for B3 ($W = 170 \text{ N}$; $i = 20\%$).

The relation of gross tractive effort and slip for B3 wheel is portrayed in Figure 3-7. That of net traction and slip is depicted in Figure 3-8. In each figure, the results of experiments and those of FE–DEM analysis are included as subfigures.

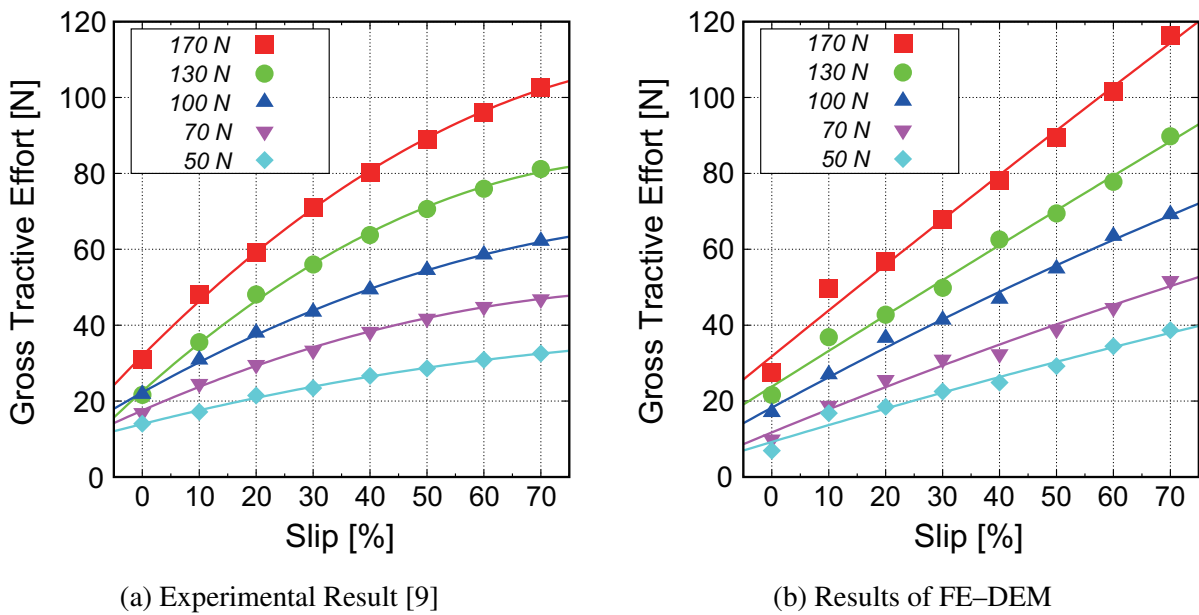


Figure 3-7: Results of gross tractive effort for B3.

In Figure 3-7 (a), the experimentally obtained result of gross tractive effort shows a wider range of variation for all cases of wheel contact loads when the wheel slip is increased. Results clarify that fitted curve for each contact load case can be expressed as a quadratic function. For the result of FE–DEM in Figure 3-7 (b), similar behavior of curves for gross tractive effort are visible, although

the result of fitting exhibits an almost linear trend. Consequently, a clear difference of gross tractive effort between the experiment and FE–DEM is apparent for wheel slip greater than 40%, especially for cases of wheel contact loads of 100 N and 170 N. However, for other ranges of wheel slippage, it might be said that the results of FE–DEM can sufficiently explain the behavior of the experimentally obtained result.

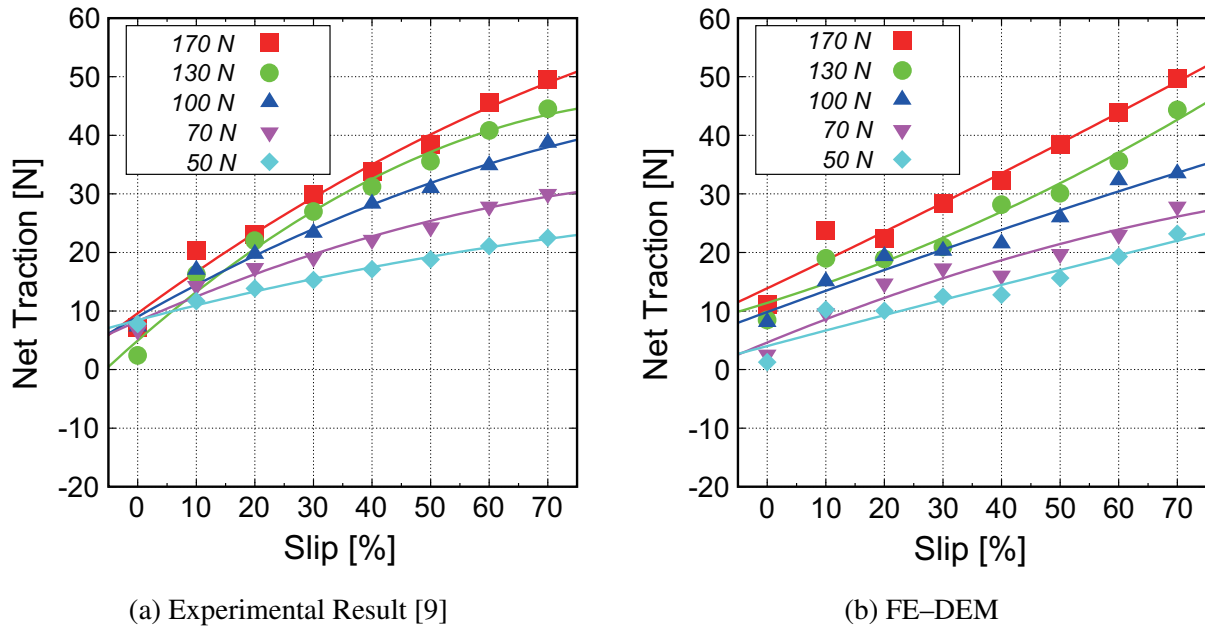
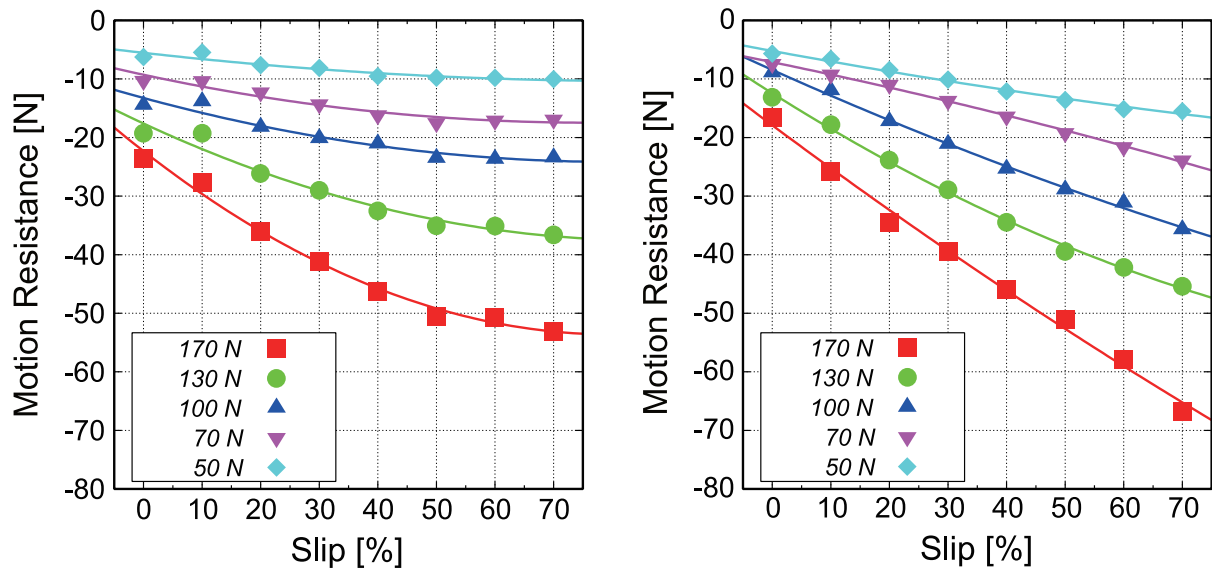


Figure 3-8: Result of net traction for B3.

For experimental net traction in Figure 3-8 (a), similar increasing behavior of curves becomes clear against the increasing wheel slip. In Figure 3-8 (b) for numerical results of net traction, the increasing result of FE–DEM is visible with the increase in wheel slippage, although fitted curves of some cases of wheel contact loads result in different behavior of the quadratic function. Although the tendency of a slight difference is apparent for the case of 0% slip in the result of FE–DEM, the result of FE–DEM for net traction might be said to have sufficient accuracy to explain the behavior of the experimentally obtained result.

The result of motion resistance between experiments and FE–DEM is presented in Figure 3-9 (a) for the experimentally obtained result, and Figure 3-9 (b) for the result of FE–DEM. By comparing Figure 3-9 (a) and (b), results of FE–DEM analysis are apparent as almost linearly increasing in absolute value as the wheel slip increases in all cases of the wheel contact load. Moreover, in both cases of Figure 3-9 (a) and (b), the motion resistance increases in absolute value with the increasing slip, which explains the increased sinkage of the wheel at a larger wheel slip. It is noteworthy that the result of motion resistance in FE–DEM is calculated from the gross tractive effort and net traction as in Eq. (3.7).



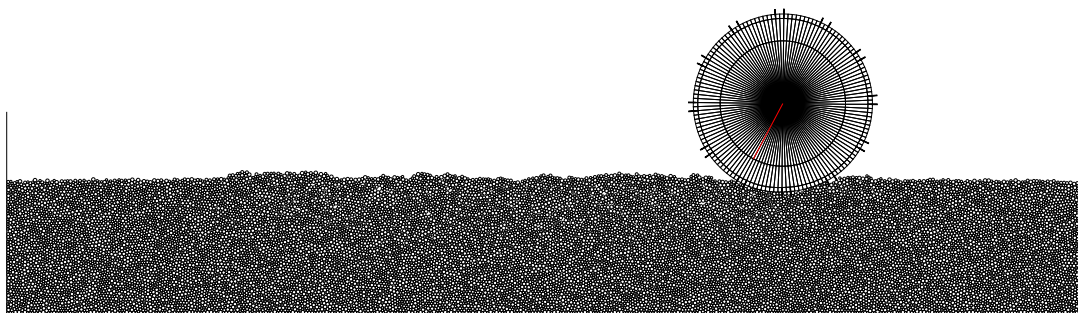
(a) Experimental Result [9]

(b) Result of FE-DEM

Figure 3-9: Result of motion resistance for B3.

B6 Wheel

Figure 3-10 presents an example of wheel and soil deformation at the end of travel of the B6 wheel with $i=20\%$ and $W=170\text{ N}$. Similar behavior of the soil surface can be regarded as in Figure 3-6 for the B3 wheel. Because the rigidity of WI for B6 wheel is greater than that of B3, the wheel deformation at the contact interface becomes small. The B6 wheel might be approximated as a rigid wheel.

Figure 3-10: Example of wheel and soil deformation for B6 ($W = 170\text{ N}$; $i = 20\%$).

The relation between gross tractive effort and wheel slip is shown in Figure 3-11. That between net traction and slippage is shown in Figure 3-12.

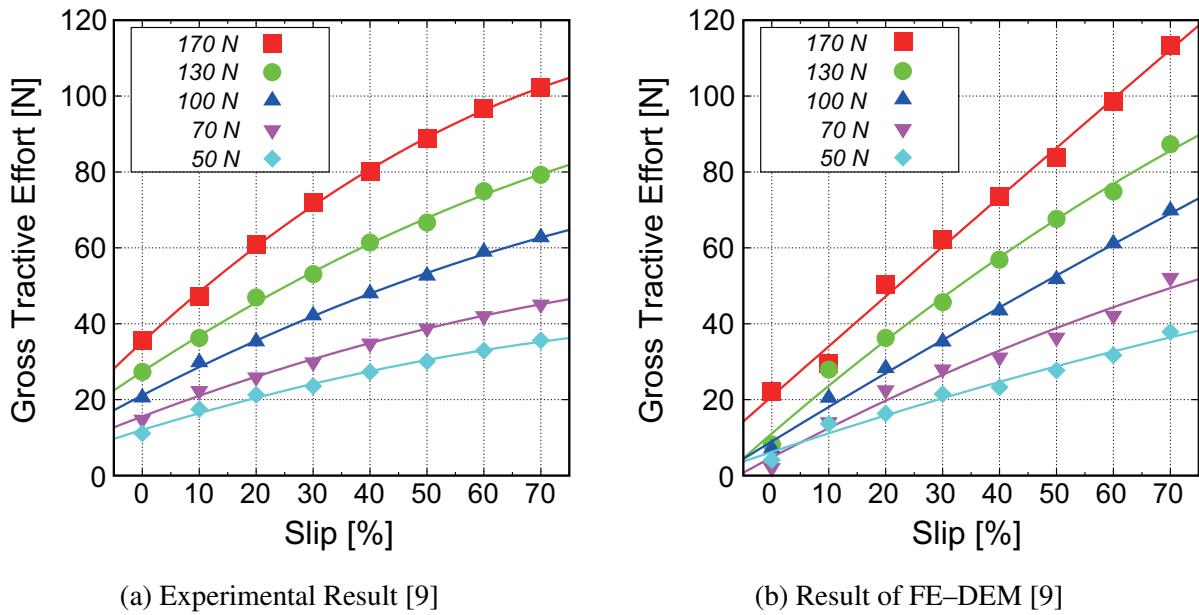


Figure 3-11: Result of gross tractive effort for B6.

As presented in Figure 3-11 (a), the experimental gross tractive effort for the B6 wheel shows similar behavior of curves to that in Figure 3-7 (a) for B3 wheel. However, the result of FE-DEM (Figure 3-11 (b)) shows smaller gross tractive effort for slippage below 30%, whereas the fitted result shows almost linear behavior in all cases of wheel contact load.

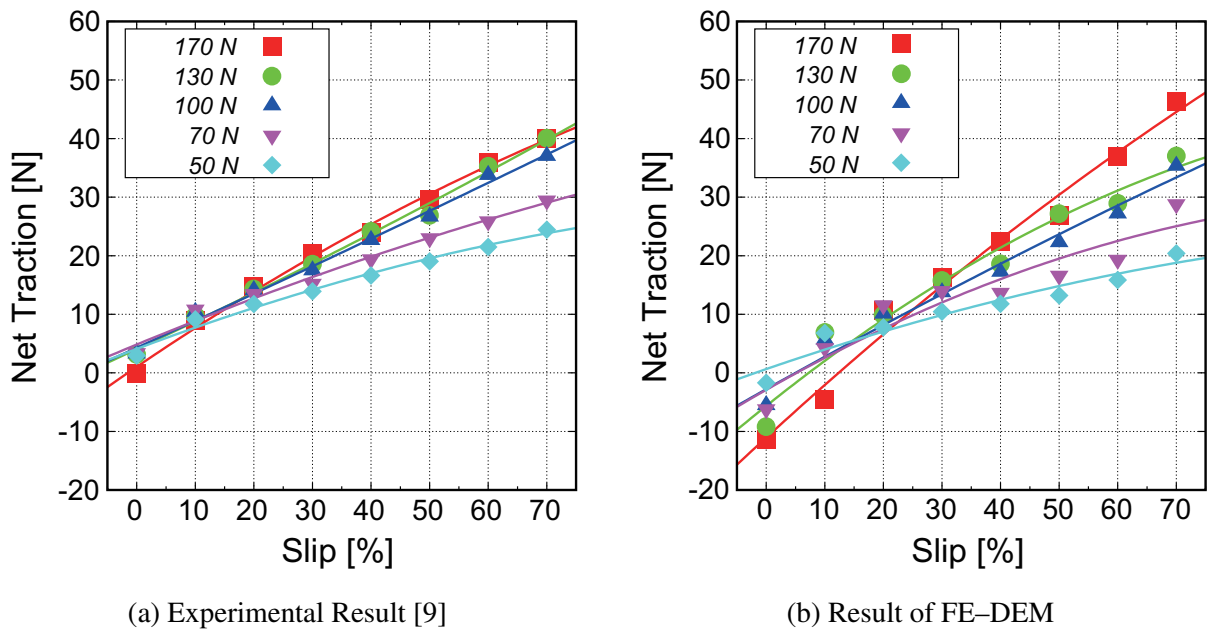


Figure 3-12: Result of net traction for B6.

The result of experiment on net traction for B6 wheel depicts rather characteristic behavior as in Figure 3-12 (a), where all fitted lines intersect at around $i=10\%$. For cases of wheel contact load greater than or equal to 100 N, the difference of net traction becomes smaller when the slip becomes greater than 20%. Similar behavior of intersecting of fitted lines is apparent in the result of FE-DEM analysis, Figure 3-12 (b), except for the condition of $W=170$ N. The rate of change in net traction per wheel slip for the result of FE-DEM becomes greater than that of the experimentally obtained result for the case of $W=170$ N.

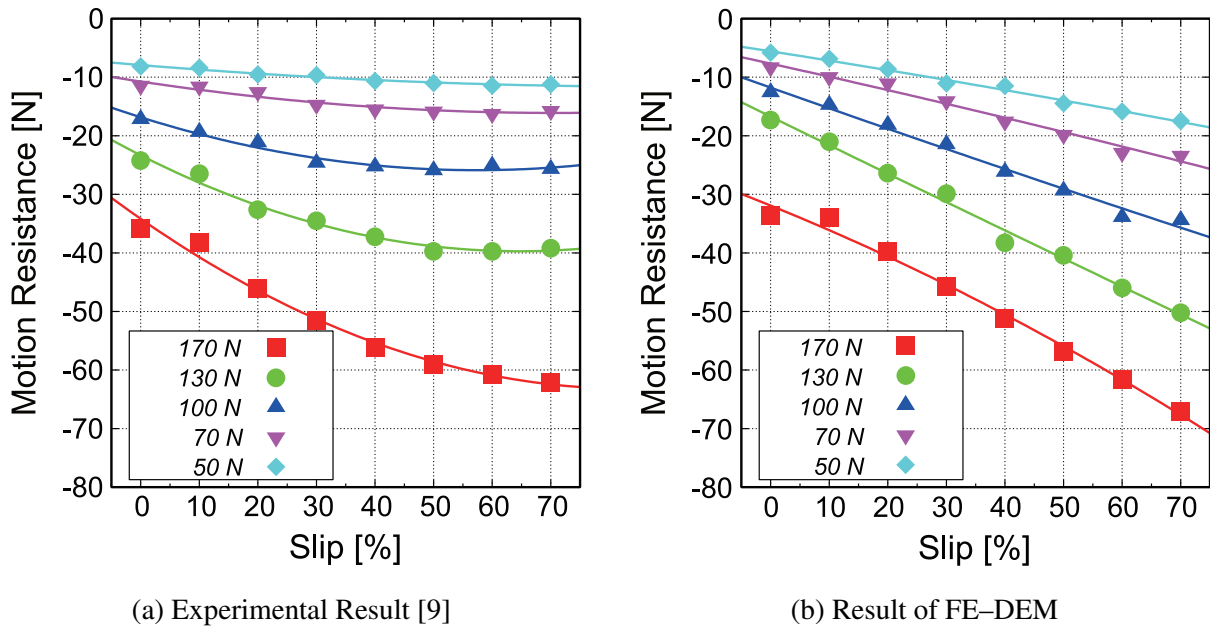


Figure 3-13: Result of motion resistance for B6.

The result of motion resistance for B6 wheel is shown in Figure 3-13. As explained already in the case of B3 wheel (Figure 3-9 (a)), the experimental result of motion resistance for B6 wheel shows a similar increase of the absolute value for all wheel contact load cases with increasing slip. Fitting by quadratic function is applicable for the experimentally obtained result with bounding motion resistance for each wheel contact load case. However, the result of FE-DEM for motion resistance can be approximated by an almost linear function with increased absolute value with increased wheel slip.

3.3.2 Discussion

As presented in Section 3.3.1, the numerical result of traction analysis for B3 wheel depicts superior net traction to that of B6 wheel within the variation of parameters investigated. Moreover, the numerical results of gross tractive effort for B3 and B6 depict a similar trend of increase with increasing slip, but smaller values of gross tractive effort became clear for smaller slip below 30% for the case of the B6 wheel. In FE-DEM analysis, the net traction is the result of analysis. The motion resistance

is the calculated result from the difference of net traction and gross tractive effort, as shown in Eq. (3.7). From comparison with tractive performance analyses for elastic wheels by parametric method [2], it is readily apparent that 2D FE–DEM in this study can more accurately predict the net traction of an elastic wheel.

The behavior of motion resistance obtained from the result of FE–DEM for two wheels as in Figure 3-9 (b) and 3-13 (b) shows a similar increase with the increase in slip, which is regarded as an improvement compared with the previous FE–DEM analysis [7]. However, when compared with the experimentally obtained result, the behavior of numerical motion resistance shows not a quadratic but a linear trend against the slip in all cases of contact load in both wheels (Figure 3-9 (b), 3-13 (b)).

To assess this difference, the comparison of sinkage of wheel is added for two wheels, as shown in Figure 3-14 and Figure 3-15.

From Figure 3-14 for B3 wheel, the result of sinkage by FE–DEM (Figure 3-14 (b)) shows an increase in the absolute value as the wheel slippage increases in all cases of wheel loads, which is qualitatively similar to the result of experiments (Figure 3-14 (a)). Moreover, it is observable that the sinkage from FE–DEM varies with the wheel load condition, as in the result of experiments in the figure. However, the numerical result of sinkage clearly becomes smaller than the experimental result in all cases of wheel loading.

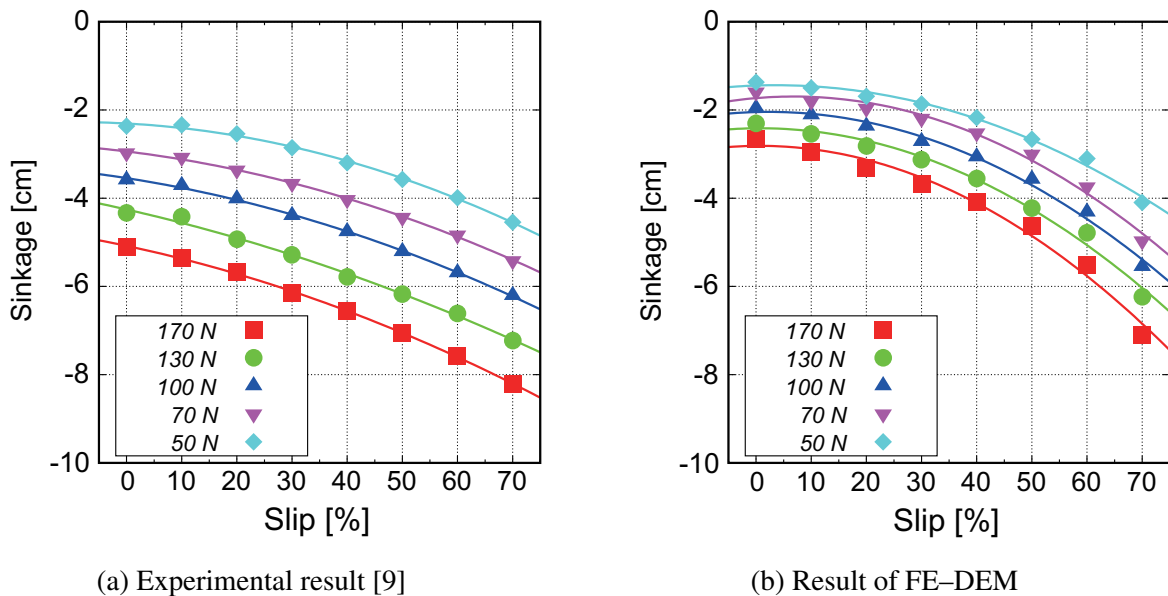


Figure 3-14: Sinkage of the B3 wheel.

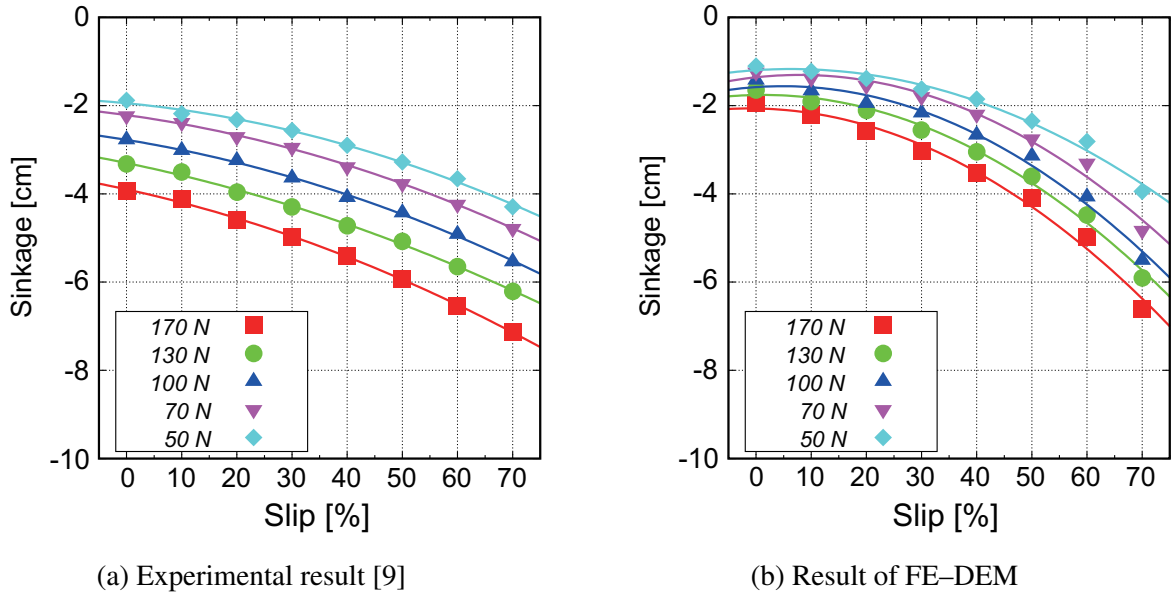


Figure 3-15: Sinkage of the B6 wheel.

In the case of the B6 wheel in Figure 3-15, similar behaviors of sinkage curves are apparent in the result of FE-DEM, as described above for the B3 wheel. The experimentally obtained result of sinkage becomes greater for the slip condition except for $i=70\%$, where the numerical sinkage might be regarded as similar to experimental results obtained in all cases of wheel load.

Moreover, comparison of Figure 3-14 and 3-15, reveals that the result of FE-DEM can explain the characteristic experimentally obtained result that a more flexible wheel (B3) has larger wheel sinkage than a more rigid wheel (B6) for cases of larger wheel contact load. Consequently, for wheel sinkage, the proposed FE-DEM has sufficient capability to analyze the sinkage of the elastic wheels that were investigated.

Finally, the wheel deflection of B3 and B6 wheels was investigated further. The wheel deflection versus wheel slip for B3 and B6 wheels under $W=170\text{ N}$ is shown in Figure 3-16 (a). In the current FE-DEM, the deflection of an elastic wheel is ascertained from the minimum length, or radius, between the FE node at the rotation center and a node on the contact surface of wheel model.

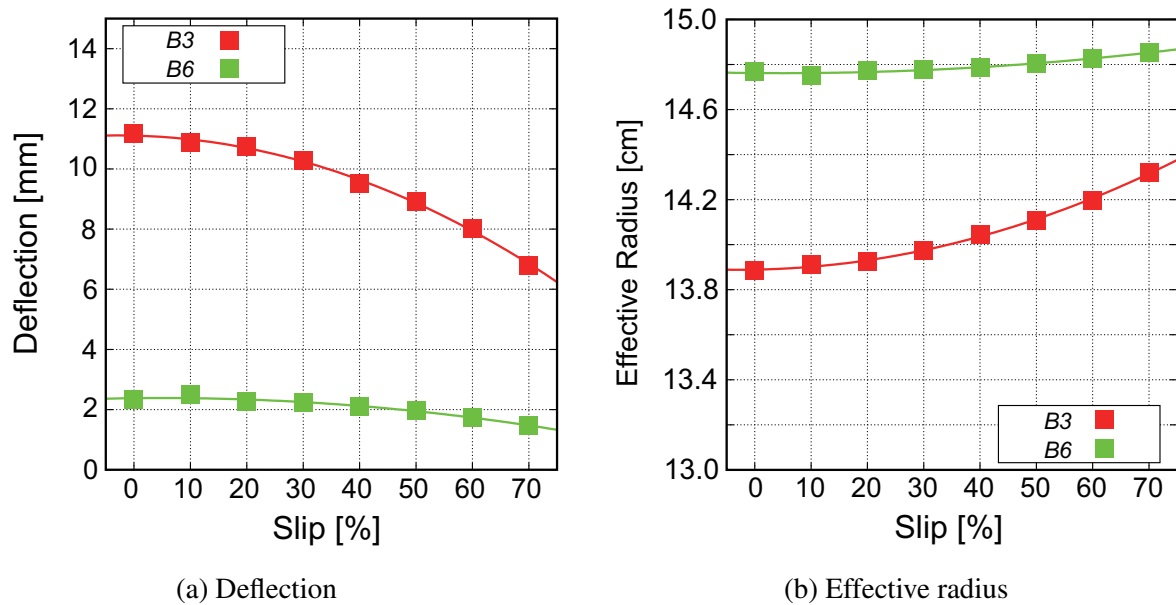


Figure 3-16: Deflection and effective radius of elastic wheels B3 and B6 under $W = 170$ N.

It is noteworthy that the deflection of a wheel from FE-DEM decreases when the slip increases, and that a flexible B3 wheel shows more noticeable reduction of deflection than a B6 wheel. This reduction derives from a normal node reaction acting on the contact surface of WS as a result of increased contact length with increasing wheel sinkage at a larger slip. Consequently, the effective radius of a wheel also increases gradually concomitantly with the reduction of wheel deflection in the case of the B3 wheel, as shown in Figure 3-16 (b).

3.4 Prediction of wheel performance on Mars using FE-DEM

By applying the developed FE-DEM program, the tractive performance of a B3 wheel on Mars can be predicted. The contact load of $W = 170$ N on Earth was corrected by the acceleration of gravity on Mars to have the vertical contact load condition of $W' = 64.4$ N, which implies the identical mass condition assumed [6]. The time period for initial consolidation of soil elements was extended from 1 s to 2.64 s, considering the reduced effect of consolidation under low gravity on Mars [6]. Time period of vertical free sinkage of the wheel was set as 2 s. The time step Δt was changed to $\Delta t = 5.0 \times 10^{-6}$ s to ensure the stable computation of FE-DEM. Other parameters were the same as those presented in Table 3-1 – 3-4.

Gross tractive effort vs. slip is shown in Figure 3-17 (a), and net traction vs. slip is in Figure 3-17 (b). Motion resistance and sinkage of wheel are shown in Figure 3-18. The results obtained on Earth are also depicted in those figures for reference.

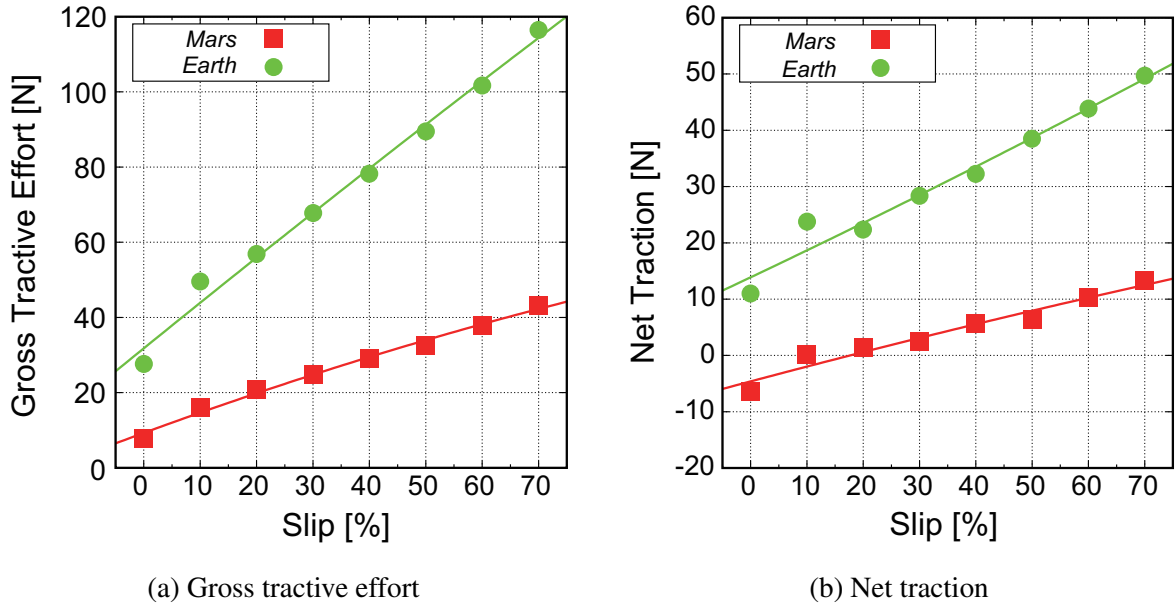


Figure 3-17: Gross tractive effort and net traction of B3 wheel on Earth and on Mars.

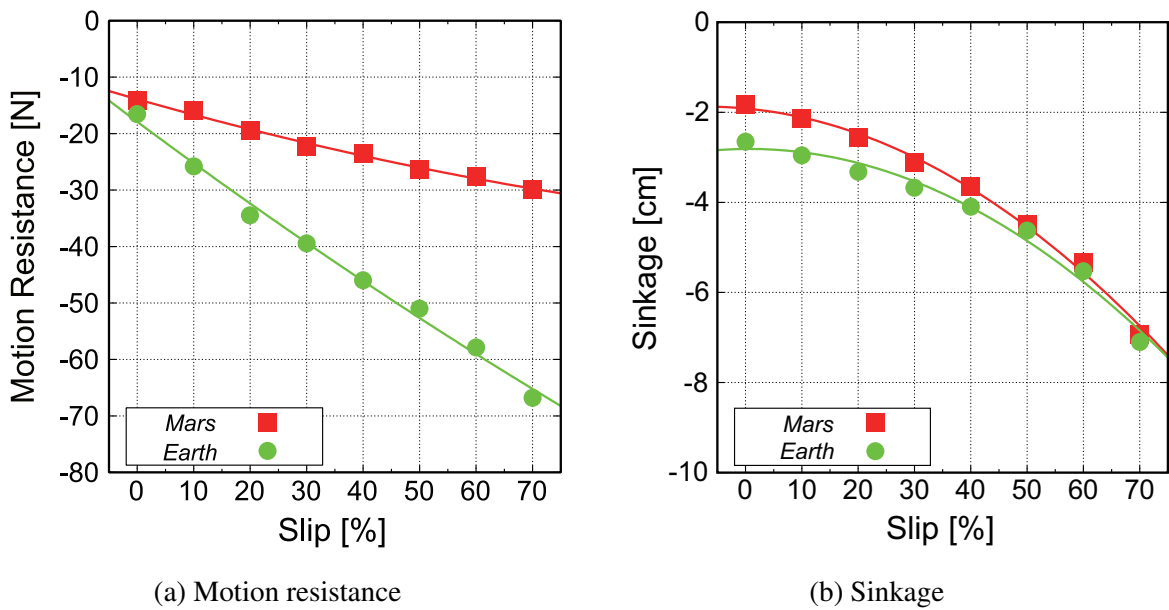


Figure 3-18: Motion resistance and sinkage of B3 wheel on Earth and on Mars.

A discussion of the gravity ratio [6] might be applied to numerical results in Figure 3-17 and 3-18 to evaluate the correctness of tractive performance using FE–DEM on Mars, although it is noteworthy that the current target wheel is an elastic wheel with no identical self-propelled condition. An effect of rolling resistance moment is included in this study.

The case of $i=60\%$ is selected, where the effect of wheel deformation can be reduced as shown in Figure 3-16. For $i=60\%$, the gross tractive effort on Earth, H_e , and that on Mars, H_m , can be found respectively as $H_e=102\text{ N}$ and $H_m=38\text{ N}$ from Figure 3-17 (a). The ratio of $H_m/H_e =$

$38/102 = 0.373$ might be regarded as similar to a rough estimation of the ratio of the acceleration of gravity: $0.378 (= 3.71/9.81)$.

When the net traction for $i = 60\%$ is investigated from Figure 3-17 (b), the ratio of the net traction on Mars and that on Earth becomes $P_{d,m}/P_{d,e} = 11/43 = 0.256$, which is clearly smaller than 0.378 if one assumes a similar linear relation of gravity ratio with respect to net traction.

The Motion resistance on Mars, R_m , was found to be $R_m = -27.5$ N, whereas that on Earth, R_e , becomes $R_e = -58$ N at the slip of $i = 60\%$ from Figure 3-18 (a). Consequently, results show that the ratio $|R_m/R_e| = 25.5/58 = 0.474$ becomes greater than the gravity ratio of 0.378 . Because the motion resistance in this study is a result of calculation by Eq. (3.7), the larger result of the ratio caused by the smaller result of net traction stated above might be understood.

Regarding the wheel sinkage shown in Figure 3-18 (b), the sinkage on Mars, z_m , can be specified as $z_m = -5.5$ cm, whereas that on Earth is obtained as $z_e = -5.75$ cm. Consequently, the ratio $|z_m/z_e| = 5.5/5.75 = 0.957$ becomes slightly smaller than 1.0 , which implies no relation with gravity acceleration. As the figure shows, the predicted sinkage on Mars shows qualitatively similar behavior to that on Earth. Both sinkages at $i = 70\%$ might be regarded as identical.

As a relative evaluation, the tractive performance of B6 wheel on Mars was also analyzed. Not all results but net traction and sinkage are presented in Figure 3-19. For a small range of wheel slip, the B3 wheel does indicate a slightly larger net traction than that for the B6 wheel (see Figure 3-19 (a)). However, the difference of net traction might be neglected for $i \geq 30\%$. As for wheel sinkage in Figure 3-19 (b), the B3 wheel sinkage becomes greater than that of B6 wheel for the slip range of $0\text{--}50\%$, but the difference of sinkage between two wheels might also be neglected for such a wheel with radius of 158 mm, inclusive of lugs. Consequently, it might be concluded that two elastic wheels, B3 and B6, produce similar net traction and sinkage on Mars according to the FE–DEM results.

Results show that the flexible structure of elastic wheel (B3) might not be effective for the generation of net traction on Mars when the identical mass condition is assumed with the contact load of $W' = 64.4$ N on Mars based on the current 2D FE–DEM.

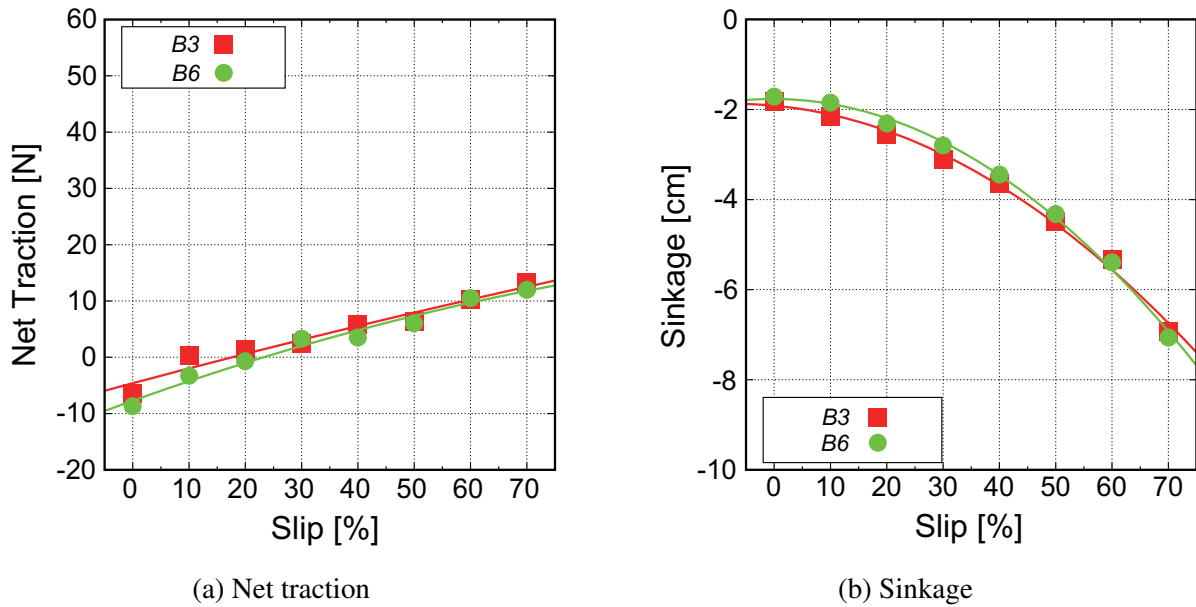


Figure 3-19: Net traction and sinkage of B3 and B6 wheels on Mars ($W' = 64.4$ N).

3.5 Conclusion

We upgraded our previously developed 2D finite element–discrete element method (FE–DEM) for application to tractive performance analysis of an elastic flexible wheel, where a new algorithm learned from a PID-controller model was introduced.

For the verification of accuracy of analysis by the FE–DEM, results of experiments on two wheels of different rigidity, B3 and B6, collected by DLR Bremen, Germany, were compared. The tractive performance analyzed by FE–DEM was found to generate similar qualitative results to those obtained by experimentation. Therefore, it was clarified that the newly developed 2D FE–DEM program is applicable as a design tool for interactive studies of an elastic wheel.

As an application of FE–DEM, the analysis of the tractive performance of an elastic wheel on Mars was attempted. The FE–DEM result was understood as adequately expressing the tractive performance of B3 wheel on Mars, but further investigation of coefficients of PID model for a drawbar pull are also expected to be necessary to estimate the relation of tractive performance and the gravity ratio on Mars accurately.

The FE–DEM result showed that a more flexible B3 wheel shows no distinguished superiority in the generation of net traction on Mars over the model B6 wheel, when the identical mass condition is assumed for the contact load condition of 170 N on Earth.

References

- [1] ESA. 2015. ExoMarsRover. <http://exploration.esa.int/mars/45084-exomarsrover/> (accessed December 23, 2018)
- [2] Favaedi, Y., A. Pechev, M. Scharringhausen, and L. Richter. 2011. Prediction of tractive response for flexible wheels with application to planetary rovers. *Journal of Terramechanics* 48: 199-213.
- [3] Freitag, D. R. and Smith ME. 1966. Center-line deflection of pneumatic tires moving in dry sand. *Journal of Terramechanics* 3 (1966) 31-46.
- [4] Matsukawa, H.. 2009. Expression of tire deformation in FE-DEM. Unpublished Bachelor of Agric. Sci. Thesis, Department of Agricultural and Environmental Engineering, Faculty of Agriculture, Kyoto University. (in Japanese)
- [5] Nakashima, H., Y. Takatsu, H. Shinone, H. Matsukawa, and T. Kasetani. 2009. FE-DEM analysis of the effect of tread pattern on the tractive performance of tires operating on sand. *Journal of Mechanical Systems for Transportation and Logistics* 2 (1): 55-65.
- [6] Nakashima, H. and T. Kobayashi. 2014. Effects of gravity on rigid rover wheel sinkage and motion resistance assessed using two-dimensional discrete element method. *Journal of Terramechanics* 53: 37-45.
- [7] Ono, T., H. Nakashima, H. Shimizu, J. Miyasaka, and K. Ohdoi. 2010. Analysis of elastic wheel performance for off-road mobile robots using FE-DEM. In: Proc. the Third IFAC International Conference Agricontrol, 61-66. (<http://dx.doi.org/10.3182/20101206-3-JP-3009.00010>)
- [8] Patel, N., R. Slade, and J. Clemmet. 2010. The ExoMars rover locomotion subsystem. *Journal of Terramechanics* 47: 227-242.
- [9] Scharringhausen, M., D. Beermann, O. Krömer, and L. Richter. 2009. Single wheel tests for planetary applications at DLR Bremen. In: Proc. 11th European Regional Conference ISTVS, Bremen. (CD-ROM)
- [10] Shinone, H., H. Nakashima, Y. Takatsu, T. Kasetani, H. Matsukawa, H. Shimizu, J. Miyasaka, and K. Ohdoi. 2010. Experimental analysis of tread pattern effects on tire tractive performance on sand using an indoor traction measurement system with forced-slip mechanism. *Engineering in Agriculture, Environment and Food* 3(2): 61-66.
- [11] Smith, W. and H. Peng. 2013. Modeling of wheel-soil interaction over rough terrain using the discrete element method. *Journal of Terramechanics* 50: 277-287.

- [12] Takatsu, Y.. 2009. Analysis for off-road mobility of tires by finite element-discrete element method. Unpublished Master of Agric. Sci. Thesis, Division of Environmental Science & Technology, Graduate School of Agriculture, Kyoto University. (in Japanese)
- [13] Wakabayashi, S., Y. Kohno, and S. Nishida. 2008. Evaluation of lowpressure mobility system for lunar vehicle. In: Preprints 26th Intl. Symposium on Space Technology and Science, Hamamatsu, 2008-k-56 (CD-ROM).
- [14] Wu, S. R. and L. Gu. 2012. Introduction to the explicit finite element method for nonlinear transient dynamics. John Wiley & Sons, Inc., Hoboken.

Chapter 4

Contact stress and tractive performance of a tire driven on dry sand

4.1 Introduction

The distribution of contact stresses at the soil–tire interface has been an important factor for assessing the tractive performance of a tire traveling on off-road terrain. An earlier report of a study by Wong [15] summarized the procedures for calculating tractive performance of a tire through the integration of normal, or radial, and tangential contact stresses over the contact interface between a tire and soil as a parametric (or semi-empirical) approach. Consequently, it is necessary to investigate normal and tangential contact stresses of off-road tires. Because the manufacturing of small and thin sensors that can be embedded in the tire tread has remained difficult, earlier studies have mostly examined the measurement of stress distribution for a rigid wheel on deformable terrain.

The normal component of contact stress reached a maximum level before the bottom dead center of the rotation axis of wheel for a positive slip of 30% [11]. Although VandenBerg and Gill [12] measured the distribution of normal contact stress by small pressure cells installed on the tire body, the tire slip was not described. The tangential stress on the contact surface remained unknown. Another report of the literature by Onafeko and Reece [7] also described that the rotation angle for maximum radial contact stress would be shifted forward from the bottom dead center as the wheel slip increased up to 41.5%. Similarly, the stress distribution of a rigid wheel traveling on sand was measured. Results showed the same forward shift of rotation angle for maximum normal contact stress with increasing slip [8]. Moreover, it is noteworthy that the result of the vertical contact load of a wheel calculated using the integration of normal and tangential stresses measured using a T-shaped sensor became less than the macroscopically measured traction performance using an L-shaped sensor installed at the support of the wheel system running on dry sand [5]. An interesting report [13] presented the conclusion that, in their experiment for a rigid wheel with sandy loam soil, the angle of rotation for maximum normal stress decreased, although that for maximum tangential

stress increased with increasing slip, and that those angles would coincide at about 75 deg, when the slip became 50%.

A two-dimensional stress sensor that can also measure tire deformation was developed by [1] and was embedded into the tire lug of a tractor tire. It is noteworthy that the distributions of normal and tangential contact stresses at the tire lug showed different behavior, where maximum normal stress appeared after the dead bottom center of the tire axle before the maximum deformation of the tire on a firm soil condition [16]. The thrust obtained by integration of tangential stress and the motion resistance by integration of normal stress respectively caused similar results of gross traction and motion resistance, which are defined by ASAE standards [17].

For measurement of precise contact stresses on a three-dimensional (3D) tire surface, Krick [3] developed a unique small triaxial sensor, 36 mm diameter and 13 mm height to obtain normal and two tangential stresses during the contact of a tire traveling on a deformable terrain. Moreover, the rotation angles for maximum normal and tangential stresses were not shifted remarkably. They remained at similar angles in 10%- and 40%-slips. Using a triaxial force sensor similar to Krick's for a tire running over silica sand, Oida et al. [6] also attempted a measurement, verifying the forward shift of rotation angle for maximum radial contact stress from the bottom dead center of the tire for slip conditions up to 60%, but the location of the angle moved backward for a slip larger than 60%. Moreover, the stress distribution at the contact surface of a tire running on sand was measured recently using a small and thin triaxial force sensor [2]. Their result showed that the gross tractive effort and net traction of a tire could be obtained qualitatively through integration of the parametric approach, although the result of contact wheel load showed decreasing trend with increasing slip.

This study was undertaken to investigate normal and tangential contact stresses of a tire running on dry sand terrain by our updated 2D FE–DEM program. A stationary averaging method for contact stresses is introduced by assuming the steady state condition of the tire travel and rigid contact mode of a tire. By comparing the integrated result with those of parametric analysis and with our earlier experimentally obtained results, the accuracy of FE–DEM for analysis of contact stresses in relation with tractive performance of the tires is then discussed. The relation between the angle of rotation of the tire and maximum normal and tangential contact stresses in FE–DEM is also investigated.

4.2 Traction performance analysis

4.2.1 Traction performance analysis using a model incorporating FE–DEM with PID control

Detail modeling and analyzing method is referred in Section 3.2.1. A tire is modeled by FEM. The soil is modeled by DEM. Every time step, contacts among DEs are checked and reaction forces are

calculated, and then the drawbar pull and wheel torque are given based on the PID automatic control as external forces to the FE nodes. Finally, each coordinate of DE and FE node is updated according to equations of motion.

Both analysis and experiment intended in this study, because V and ω in Eq. (3.8) can be controlled independently under the forced-slip condition, it can be realized that constant slip ratio and steady state condition is maintained except for acceleration period just after start of traveling. In the analysis, V and ω are adjusted by adding the traction load and torque respectively from Eq. (3.2) and (3.3). As in experiment [10], they can be controlled by independent AC motors, in which V is often varied to obtain a target slip i under constant ω .

The traction performance indicator; gross tractive effort H , net traction P_d and running resistance R , which should be assessed against slip, can be obtained from the Eq. (3.5) ~ (3.7). In these equations, wheel torque T and drawbar pull P come from the result of PID controller ruled by Eq. (3.2) and (3.3). The contact reaction at the soil–tire interface is not used directly to obtain the gross tractive effort and running resistance, but a method similar to that of the experiments is applied in the current FE-DEM model.

4.2.2 Normal and tangential contact stresses in FE–DEM

When a tire travels on deformable soil, let a front or entry angle of contact be θ_1 and an end angle of contact be θ_2 . The angle for bottom dead center becomes $\theta = \pi/2$, when the origin of the rotation angle is taken as the direction of tire travel with the positive angular velocity in clockwise rotation as shown in Figure 4-1. The positive direction of each contact stress is also shown in the figure.

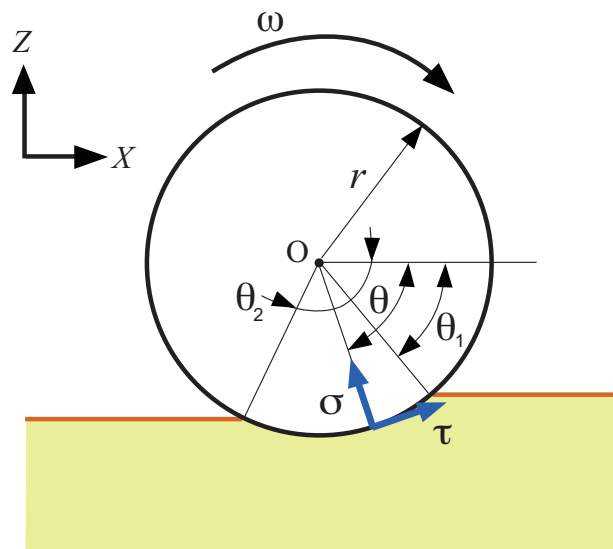


Figure 4-1: Normal and tangential contact stresses and rotation angle of a tire.

In FE–DEM, normal and tangential contact reactions can be obtained easily as a result of

contact between soil DE elements and wheel FE elements. Either contact forces on the soil discrete elements or reaction forces on nodes of the FE element at the tire surface might be used to calculate normal and tangential stresses at the contact surface between the tire and soil models. In terms of resolution of contact reactions with respect to the angle of rotation, the former contact reactions obtained by soil discrete elements should be used because the scale of discrete elements is smaller than that of finite elements.

It is noteworthy that the contact forces tend to exhibit vibratory response with high frequency caused by the instantaneous change of contact mechanism between DEM soil elements and/or between elements of soil DEM and tire FEM in a small time step of explicit integration of the equations of motion. To obtain more smoothed result of contact forces, a fast and simple averaging of normal and tangential forces is introduced in this study.

First, the rotational angle for lower half of tire, i.e. $0 \leq \theta \leq \pi$ [rad], is divided by 1000 to define a virtual infinitesimal tread segment $dl = r d\theta = r\pi/1000$ that corresponds to half the arc of the tire circumference in total, and overlapped with tread part of tire FEM elements. A contact reaction on the tire from soil will be added on a corresponding k -th virtual segment $dl(k)$ which is expressed as $dl(k) = r d\theta$ where $k = 1, \dots, 1000$, once the contact of soil DEM is observed at the angle of rotation of tire θ , assuming the stationary rotation and translation of the tire in the forced slip condition.

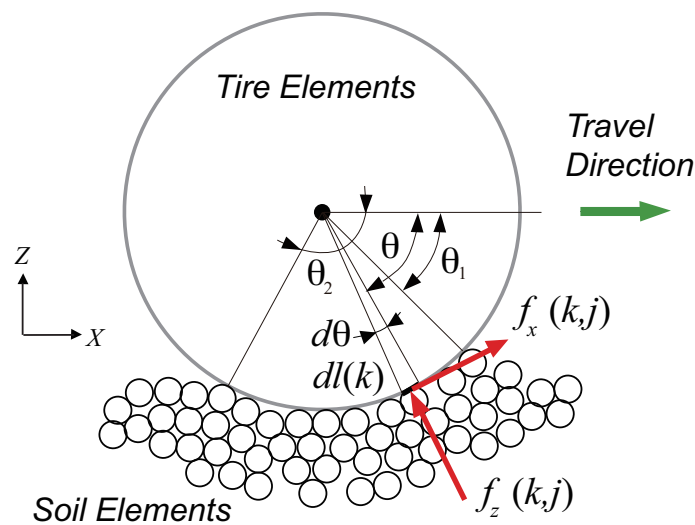


Figure 4-2: Contact forces on a virtual segment $dl(k)$ overlapped with the tire tread part.

The virtual segments would not rotate, but would only translate with the tire throughout the analysis with the assumption of stationary condition of tire locomotion where the sinkage of tire is kept constant. Consequently, each virtual segment might be understood as a summation unit of normal and tangential forces at the corresponding angle of rotation of the tire. Figure 4-2 portrays a k -th segment $dl(k)$ on the lower semicircle of the tire surface. The normal and tangential contact reaction are acting on that part by a contacting soil DEM element.

Once the contact between soil element and tire element is observed in a time integration step of FE–DEM, normal contact force $F_z(k)$ and tangential contact force $F_x(k)$ are calculable respectively as follows through averaging by the number of time steps observed:

$$F_z(k) = \sum_{t=t_0}^{t_m} \left(\sum_{j=1}^{n_c^k} f_z(k, j) \right) / (t_m - t_0 + 1) \quad (4.1)$$

$$F_x(k) = \sum_{t=t_0}^{t_m} \left(\sum_{j=1}^{n_c^k} f_x(k, j) \right) / (t_m - t_0 + 1) \quad (4.2)$$

where t_0 and t_m respectively stand for the beginning time step and the end time step of data collection in FE–DEM, n_c^k denotes the total number of contacts of soil DEM on the k -th segment, and $f_z(k, j)$ and $f_x(k, j)$ respectively stand for the normal and tangential contact force calculated at a contact j ($j = 1, n_c^k$) from the soil DEM element on the segment.

In this way, averaged datasets of $F_z(k)$ and $F_x(k)$ are obtainable for all segments for the lower half tire circumference against tire locomotion with a slip condition. Figure 4-3 depicts the relation of a stationary virtual segment $dl(k)$ at time steps between t_0 and t_m .

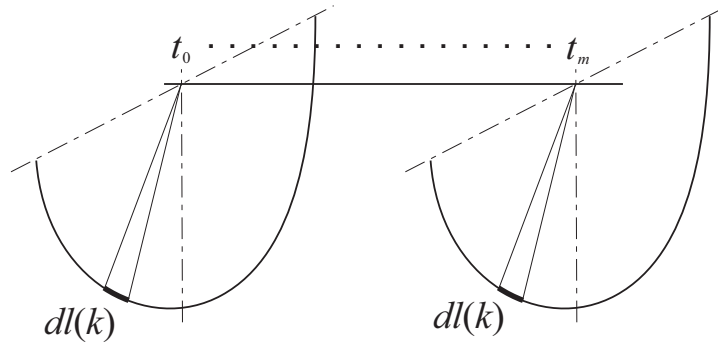


Figure 4-3: A stationary segment for summation of contact forces with respect to time stepping.

The contact period of tire to soil can be found as extracting non-zero entry of forces in the array for $F_z(k)$ or $F_x(k)$. The rotation angle θ can be obtained simply as $\theta = (k - 1/2)\pi/1000$ [rad] using the index k , where the angle θ is measured at the center of each segment length.

Normal and tangential stresses in FE–DEM are then calculated by dividing the contact reaction of Eqs. (4.1) and (4.2) with the corresponding rectangular segment area, $brd\theta$, where b is the contact width of tire and $rd\theta$ is the length of each segment.

4.2.3 Tractive performance analysis using a parametric approach

According to the parametric approach, the tractive performance of a tire with rigid contact mode is calculable by normal stress $\sigma(\theta)$ and tangential stress $\tau(\theta)$ distributed along the contact arc length [15].

The vertical contact load of tire W can therefore be calculated as

$$\begin{aligned} W &= br \int_{\theta_1}^{\pi/2} (\sigma(\theta) \sin \theta + \tau(\theta) \cos \theta) d\theta \\ &+ br \int_{\pi/2}^{\theta_2} (\sigma(\theta) \sin \theta - \tau(\theta) \cos \theta) d\theta \end{aligned} \quad (4.3)$$

where b signifies the contact width of tire equivalent with tread width in case of two-dimensional analysis, r denotes the undeflected tire radius, θ_1 denotes the entry angle of contact measured from the longitudinal horizontal axis, and θ_2 represents the exit angle of contact measured from the longitudinal horizontal axis.

The gross tractive effort H becomes the following.

$$H = br \int_{\theta_1}^{\theta_2} \tau(\theta) \sin \theta d\theta \quad (4.4)$$

Similarly, the running resistance of tire R is expressed as an integral of tangential stress, as

$$R = br \int_{\theta_1}^{\theta_2} \sigma(\theta) \cos \theta d\theta. \quad (4.5)$$

Consequently, the net traction P_d in the parametric analysis can then be calculated as a difference of H and R , such that

$$P_d = H - R, \quad (4.6)$$

which directs forward and is equal to the drawbar pull P acting rearward on the tire rotation axle.

It is noteworthy that the negative tangential stress contributes to the running resistance, which can often be observed in a small slip of a tire. Moreover, the normal stress at larger rotation angle than 90 deg partly contributes to the gross tractive effort because the horizontal component of normal stress is directed forward. These cases are also considered in this study, although they are not expressed explicitly in Eqs. (4.4) and (4.5).

4.2.4 Input parameters in FE–DEM analysis

Previous experimental conditions [10, 2] are considered in FE–DEM. The nominal size of the tire is 165/60R13, for which the tire diameter is 535 mm and the tire width is 170 mm. Consequently, the length of a virtual segment ($rd\theta$) on the target tire is 0.84 mm. The tire rotates with constant circumferential velocity of 97.6 mm/s. The translation velocity is varied to obtain the prescribed slip condition of -5, 1, 7.5, 22, 37.5, and 55% as in the experiments. It is noteworthy that the tire has no tread pattern, and is therefore classified as smooth treaded. Contact load of tire is 980 N.

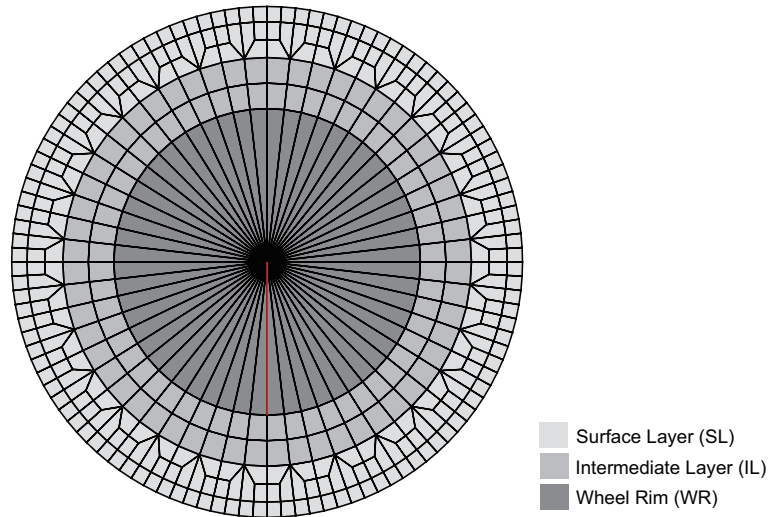


Figure 4-4: 2D FE mesh configuration for a tire.

FE mesh configuration for the tire model is shown in Figure 4-4, where three tire components are assumed: wheel rim (WR), intermediate layer (IL), and surface layer (SL). The total number of FE elements is 448. The total number of nodes is 477. Fine mesh design at the tread part is intended to increase the accuracy of contact detection. Because the numerical analysis is in 2D, the width data are used solely for calculation of the contact area.

All input parameters for FE–DEM are presented in Tables 4-1 to 4-4. The virtual soil bin size is 1.8 m long. The tire will horizontally travel 0.7 m from the origin of travel set at 0.5 m from the left edge of the soil bin. The soil bin is filled with soil DEs, the parameters of which are presented in Tables 4-2. Contact model used in DEM is Voigt model, where a spring and a damper are connected in parallel.

For simplicity, the layered structure of bottom soil using FEM is not introduced in this study. Total number of soil DEs is reduced after consolidation process because of the horizontal surface of soil is prepared by removing those soil elements over the target soil height.

The tire can be assumed as rigid contact mode under the given experimental loading condition with inflation pressure of 140 kPa and dry sand [10, 2].

Table 4-1: Parameters for Tire FEM

	WR	IL	SL
Young's Modulus [MPa]	200.0	0.3	1.5
Poisson's Ratio [-]	0.3	0.49	0.49
Element Density [kg/m ³]	3000.0	1000.0	1000.0
Width [m]	0.01	0.17	0.17
Damping Coeff. [N·s/(m·kg)]	1.0	1.0	10.0

NB) WR, wheel rim; IL, intermediate layer; SL, surface layer

Table 4-2: Parameters for Soil DEM

Number of DEM Elements	31084
Number of DEM Elements After Consolidation	30631
Elemental Radius [mm]	1.6, 2.0, 2.4 (3:2:1)*
Time Step [s]	1.25×10^{-6}
Elemental Density [kg/m ³]	2600
Width of Element [m]	0.17
Factor on Rolling Resistance	2.0

*N.B.) Ratio by the number of DEM elements

The simulation of tractive performance comprises the following three modes: (i) consolidation by the weight of soil DEs within soil bin for 1 s, (ii) free sinkage of wheel FEs onto the soil surface until vertical contact reaction of the wheel reaches the contact load of the wheel for 1 s, and (iii) wheel travel mode with a PID control model under a forced slip condition. It is noteworthy that the acceleration period of 1 s is first applied in the wheel travel mode.

For each mode, separated computer program was used, so that the effective development of analysis can be realized while reducing the computational time of modes (i) and (ii). For this reason, the single result of tractive performance is obtained for the given slip condition using the same configuration of FE and DE obtained after mode (ii) above.

After the mode (i), the bulk density of soil model in the soil bin became 2195 [kg/m³], and the porosity and the void ratio could be obtained as 0.1557 and 0.1844 respectively.

Table 4-3: Parameters for FE-DEM

	DE-DE	DE-Wall	DE-FE
Normal Spring Const. [N/m]	5.0×10^5	5.0×10^5	5.0×10^5
Tangential Spring Const. [N/m]	1.25×10^5	1.25×10^5	1.25×10^5
Friction Coeff. [-]	0.6	0.4	0.5
Friction Coeff. at Consol. [-]	0.0	0.5	NA

Table 4-4: Parameters for the PID control model in FE-DEM

	<i>P</i> -term	<i>I</i> -term	<i>D</i> -term
Drawbar Pull	1.0×10^6 [N/m]	1.0×10^4 [N/(ms)]	1.0×10^4 [N s/m]
Torque	1.0×10^5 [Nm/rad]	1.0×10^3 [Nm/(rad s)]	1.0×10^3 [Nm s/rad]

Parameters listed in Table 4-3 and 4-4 were found using preliminary computation. Those parameters on *I*-terms and *D*-terms in PID model (Table 4-4) are not so sensitive as on the *P*-term

[4].

Averaging of contact reactions summarized above was applied for those results of contact forces in FE–DEM from 0.9 m to 1.2 m long the left edge of the model soil bin.

4.3 Results and discussion

4.3.1 Soil behavior under a traveling tire

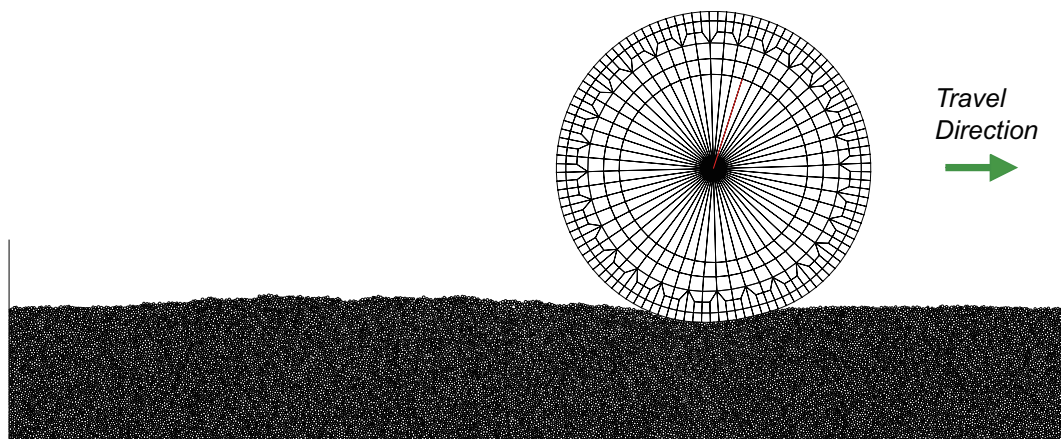


Figure 4-5: Example of soil behavior under tire travel ($i = 22\%$).

Figure 4-5 presents an example of soil behavior under a traveling tire with slip of 22%. The soil surface after passage of the tire is clearly disturbed by the uplift of soil as a result of slipped locomotion. Although it is assumed that the tire model contacts with the soil as the rigid contact mode, the slight deformation at intermediate and surface layers of the tire is also observable. As the figure shows, it is noteworthy that the entry angle of contact becomes $\theta_1 \simeq 65$ deg and that the exit angle of contact is $\theta_2 \simeq 105$ deg.

4.3.2 Normal and tangential contact stresses

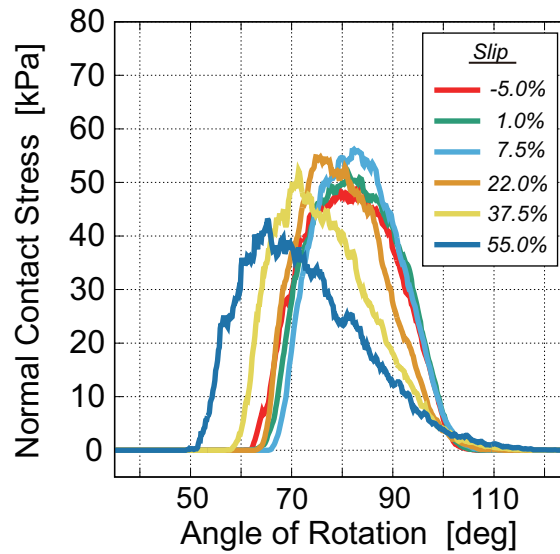


Figure 4-6: Normal contact stress in FE-DEM.

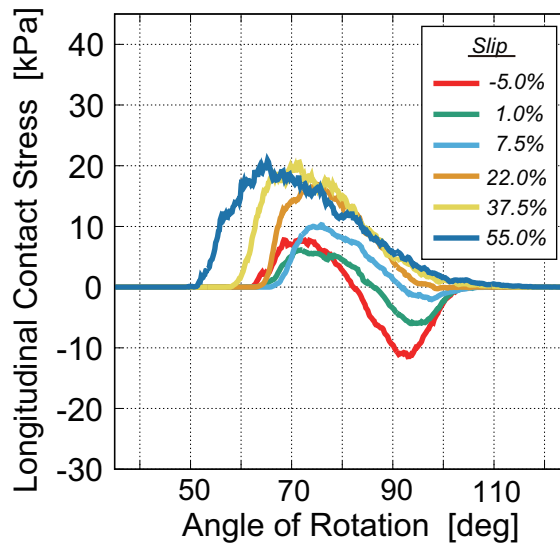


Figure 4-7: Tangential contact stress in FE-DEM.

Numerical results of normal and tangential contact stresses against the angle of rotation of the tire for various slip conditions are shown in Figure 4-6 and 4-7. In both figures, the period of angle during the contact of the tire with soil increases for 7.5% or greater slip of the tire. These behaviors correspond with the increased sinkage for a larger slip under a driven tire condition. Moreover, it is apparent that the peak, or maximum, normal contact stress shows decreasing trend when the slip increases from 7.5% in Figure 4-6.

However, an increasing trend is observed for maximum tangential contact stress with the increase of 7.5% or larger slip of the tire. Negative tangential stress is also apparent for slip of smaller than or equal to 7.5% in Figure 4-7, which is a similar result to those obtained from experiments [2].

4.3.3 Angle of rotation for maximum contact reaction

The result of angle of the tire rotation for maximum contact reactions with respect to slip obtained by FE–DEM is shown in Figure 4-8. In the figure, the red circle markers for the beginning of contact express the entry angle. The blue square markers for the end of contact depict the exit angle. The purple crossed markers show the angle of maximum tangential contact reaction, and green diamond markers imply the angle of maximum normal contact reaction.

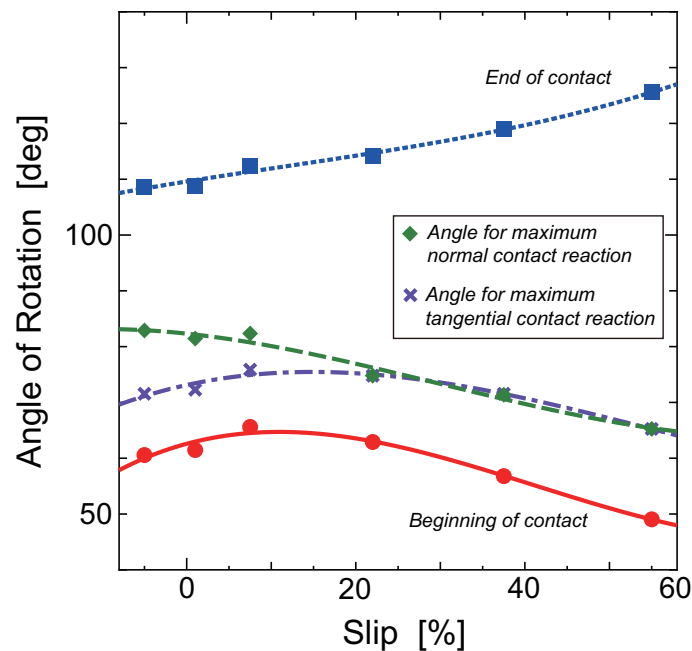


Figure 4-8: Angle of rotation for maximum contact forces from FE–DEM.

Each data set is also fitted with cubic function respectively in the figure, where the red solid curve for the beginning of contact, the purple dot-dashed curve for the maximum tangential contact reaction, the green dashed line for the maximum normal contact reaction, and the blue dotted curve for the end of contact.

A forward shift of rotation angle for the maximum normal contact reaction can be seen clearly up to slip of 55% in Figure 4-8, which is also reported for experimental results [2]. For slip of 22% or larger, similar behavior is observable for the angle of maximum tangential contact reaction in the figure. It is noteworthy that from the tire slip of 22% or larger, the angle for maximum tangential reaction obtained from FE–DEM (Figure 4-8) shows almost the same behavior of angle of rotation as the angle for the maximum normal reaction in the figure. This characteristic behavior of approaching angles of rotation for maximum normal and tangential contact forces, or stresses, for higher slip was

similarly described in reports of previous studies [8, 13]. The numerical result of the exit angle of contact in Figure 4-8 may be approximated as a linear function, instead of a cubic function that was shown in the experimentally obtained result [2]. This difference might result from the scattered data in measurement because the same angle of rotation for maximum normal stress and maximum tangential stress could not be obtained from results of experiments.

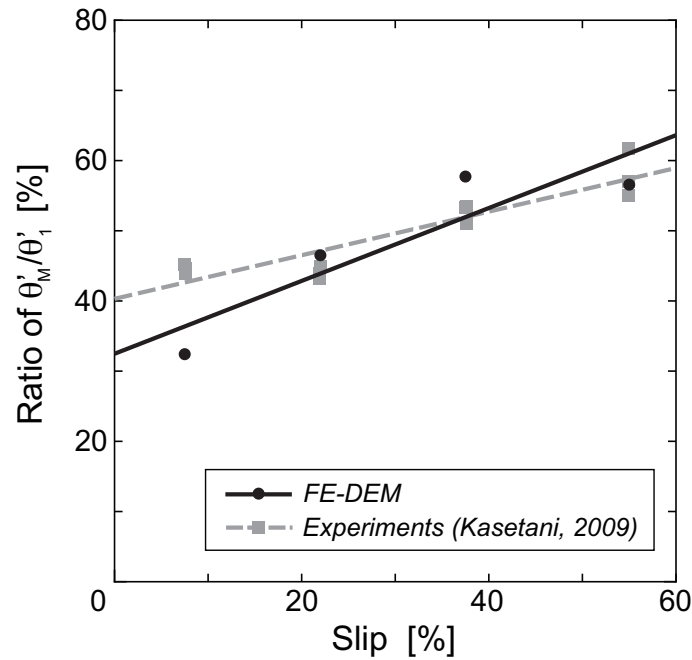


Figure 4-9: Relative position of maximum radial force with slip.

When the entry angle, θ_1 , and the rotation angle for maximum normal contact reaction, θ_M , are converted for measurement from the dead bottom center basis as θ'_1 and θ'_M , respectively, as described in the previous report [14], and the relation of the ratio θ'_M/θ'_1 against the slip can be drawn as in Figure 4-9, where black circle markers are the result of FE–DEM. The black line represents the approximated linear line. Gray square markers show the result of experiments [2] with its linearly fitted dashed line. In the figure, the range of slip is selected from 7.5% so that the driven condition of the tire can be investigated.

The result of FE–DEM may be expressed by a linear function against slip with a gradient of 0.519 whereas that of experiments with a gradient of 0.311. The difference might come from the insufficiency in 2D analysis for small slip cases. It is noteworthy that the gradient from experiments in the figure is similar to the result of sand, 0.32, as shown in [14].

4.3.4 Tractive performance

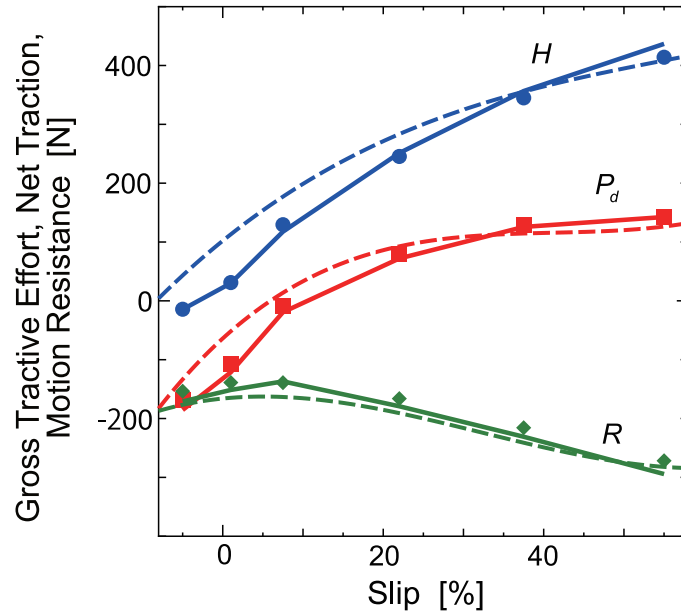


Figure 4-10: Tractive performance by FE-DEM.

Figure 4-10 depicts the result of tractive performance of the tire. In the figure, the result obtained from a model incorporating FE-DEM with PID control is shown as colored solid lines, whereas the result from integration of numerical contact stresses by parametric analysis is shown as solid markers. Blue color represents the gross tractive effort H , red implies net traction P_d , and green expresses the running resistance R in Figure 4-10. For reference, the experimentally obtained result of tractive performance using a dry filter sand is also shown with dashed lines fitted by a cubic function with the same color combination [9].

The difference between the result of tractive performance obtained using a model incorporating FE-DEM with PID control and the result of parametric analysis (as in Eqs. (4.4), (4.5) and (4.6)) calculated using contact stresses from FE-DEM is not so large against the slip, which implies that the current FE-DEM analysis with the proposed averaging method might be applicable in calculating contact stresses at the tire-soil interface with sufficient accuracy.

Regarding the comparison between the result of FE-DEM and that of previous experiments, it is noteworthy that the result of FE-DEM analysis does not coincide with the result of experiments on gross tractive effort and net traction for a smaller range of slip. Gross tractive effort of FE-DEM becomes smaller than that of experimental result for a smaller slip range of -5, 1, and 7.5%. Moreover, similar behavior of net traction of FE-DEM is apparent at the same slip range. When the motion resistance is calculated by Eq. (3.7), the difference in gross tractive effort and that in net traction become canceled as a result of subtraction. Thus, the difference in motion resistance is not so evident for the same slip range. Consequently, the result obtained using a model incorporating

FE–DEM with PID control model might be said to have sufficient accuracy in expressing tractive performance of the tire running on dry sand.

4.3.5 Contact load

The relation of the contact load W against slip is depicted in Figure 4-11. The contact load was kept unchanged in previous experiments, as shown by the solid dark gray line in figure [10]. The result of contact load by Eq. (4.3) using the contact stresses obtained in FE–DEM is shown in black circle markers in the figure. Slight decrease of contact load against the increase of slip is clearly seen, but the result from FE–DEM becomes similar to the experimental contact load condition of 980 N.

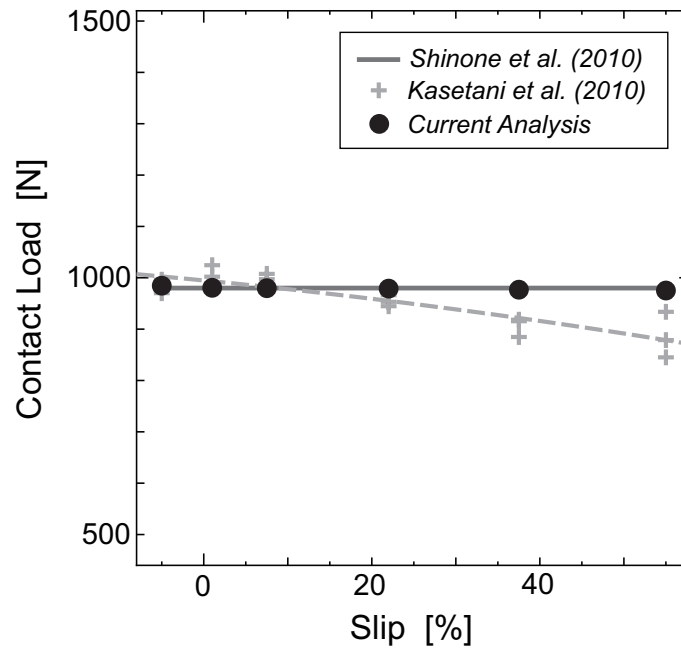


Figure 4-11: Result of contact load.

However, if we apply the parametric analysis as in Eq. (4.3) based on the experimental contact stresses, then the contact load decreased with the increase of slip, as shown by a dashed light-gray quadratic approximation [2]. This run-off result of contact load is expected to derive from an error in either normal or tangential measurement which might result from the effect of fixation of tri-axial force sensor on the surface of the tire rubber [2] or from a result of excessive reduction of soil bulk density caused by the increased action of tangential force at the tire surface, as reported by [5], but the detailed investigation is beyond the scope of the present study.

4.4 Conclusion

By assuming stationary travel of the off-road tire and a rigid contact mode, normal and tangential contact stresses are calculable in our in-house 2D FE–DEM code with PID control by introduction of averaging over virtual translating segments at the lower half of the tire.

The integration of normal and tangential contact stresses with respect to the angle of rotation was applied to calculate the vertical contact load, gross tractive effort, net traction, and running resistance of the tire using parametric (or semi-empirical) analysis. The results of tractive performance obtained through parametric analysis were found to resemble those of tractive performance obtained directly through FE–DEM analysis. A forward shift of the consistent angle of rotation for maximum normal contact stress and that for maximum tangential contact stress with the increase of slip from 22% was also observed in the results of FE–DEM.

References

- [1] Burt, E. C., R. K. Wood, and A. C. Bailey. 1987. A three-dimensional system for measuring tire deformation and contact stresses. *Trans. ASAE* 30(2): 324-327.
- [2] Kasetani, T., H. Nakashima, H. Shinone, H. Shimizu, J. Miyasaka, and K. Ohdoi. 2010. Tri-axial contact reaction at the tire-soil interface. *Engineering in Agriculture, Environment and Food* 3(1): 14-19.
- [3] Krick, G.. 1969. Radial and shear stress distribution under rigid wheels and pneumatic tires operating on yielding soils with consideration of tire deformation. *Journal of Terramechanics* 6: 73-98.
- [4] Nishiyama, K., H. Nakashima, T. Yoshida, T. Ono, H. Shimizu, J. Miyasaka, and K. Ohdoi. 2016. 2D FE–DEM analysis of tractive performance of an elastic wheel for planetary rovers. *Journal of Terramechanics* 64: 23-35.
- [5] Nohse, Y., K. Hashiguchi, M. Ueno, T. Shikanai, H. Izumi, and F. Koyama. 1991. A measurement of basic mechanical quantities of off-the-road traveling performance. *Journal of Terramechanics* 28 (1991) 359-370.
- [6] Oida, A., A. Satoh, H. Itoh, and K. Triratanasirichai. 1991. Three-dimensional stress distributions on a tire-sand contact surface. *Journal of Terramechanics* 28: 319-330.
- [7] Onafeko, O. and A. R. Reece. 1967. Soil stresses and deformations beneath rigid wheels. *Journal of Terramechanics* 4: 59-80.

- [8] S. E. Shamay. 1971. Normal and shear stress distribution under a rigid wheel in dry sand. Davidson Laboratory Report SIT-DL-71-1554, Stevens Institute of Technology, Hoboken, NJ, USA.
- [9] Shinone, H.. 2009. Improvement of an indoor traction measurement system based on a forced slip mechanism. Unpublished Master of Agricultural Sciences Thesis, Division of Environmental Science & Technology, Graduate School of Agriculture, Kyoto University. (in Japanese)
- [10] Shinone, H., H. Nakashima, Y. Takatsu, T. Kasetani, H. Matsukawa, H. Shimizu, J. Miyasaka, and K. Ohdoi. 2010. Experimental analysis of tread pattern effects on tire tractive performance on sand using an indoor traction measurement system with forced-slip mechanism. *Engineering in Agriculture, Environment and Food* 3(2): 61-66.
- [11] Uffelmann, F. L.. 1961. The performance of rigid cylindrical wheels on clay soil. In: Proc. 1st International Conference on the Mechanics of Soil-Vehicles Systems, Turin.
- [12] VandenBerg, G. E., and W. R. Gill. 1962. Pressure distribution between a smooth tire and the soil. *Trans ASAE* 5(2): 105-107.
- [13] Wanji, S., T. Hiroma, Y. Ota, and T. Kataoka. 1997. Prediction of wheel performance by analysis of normal and tangential stress distributions under the wheel-soil interface. *Journal of Terramechanics* 34: 165-186.
- [14] Wong, J. Y. and A. R. Reece. 1967. Prediction of rigid wheel performance based on the analysis of soil-wheel stresses—Part 1. Performance of driven rigid wheels—. *Journal of Terramechanics* 4: 81-98.
- [15] Wong, J. Y.. 2010. *Terramechanics and off-road vehicle engineering*, Second Edition. Butterworth-Heinemann, Amsterdam.
- [16] Wood, R. K. and E. C. Burt. 1987a. Soil-tire interface stress measurements. *Trans. ASAE* 30(5): 1254-1258.
- [17] Wood, R. K. and E. C. Burt. 1987b. Thrust and motion resistance from soil-tire interface stress measurements. *Trans. ASAE* 30(5): 1288-1292.

Chapter 5

FE-DEM with interchangeable modeling for traction analysis

5.1 iFE-DEM: FE-DEM interchangeable model

5.1.1 Outline of iFE-DEM

In FE-DEM, the tire and bottom soil layer are modeled by FEM and soil DEM modeling is applied for the top soil layer [4, 5]. It is assumed that elastic and inelastic soil behaviors can primarily be expressed by FEM and DEM, respectively. For a simple explanation of the idea behind iFE-DEM, the following algorithm in this study is based on 2D analysis; a four-node isoparametric element is used for the FEM soil model.

For typical soil-tire interaction, it is assumed that the soil DEM region is limited to the zone of influence under or near the tire-soil contact region and that the soil model in the other region can be discretized by larger FEM elements, as shown in Figure 5-1. The highlighted areas on either side of the DEM soil model in the figure are the target zones in which the element conversion from FEM to DEM in front of the tire and from DEM to FEM behind the tire is occurring as the tire moves from left to right. Calculation of the contact reaction at the boundaries between DEM and FEM is similar to that for conventional FE-DEM.

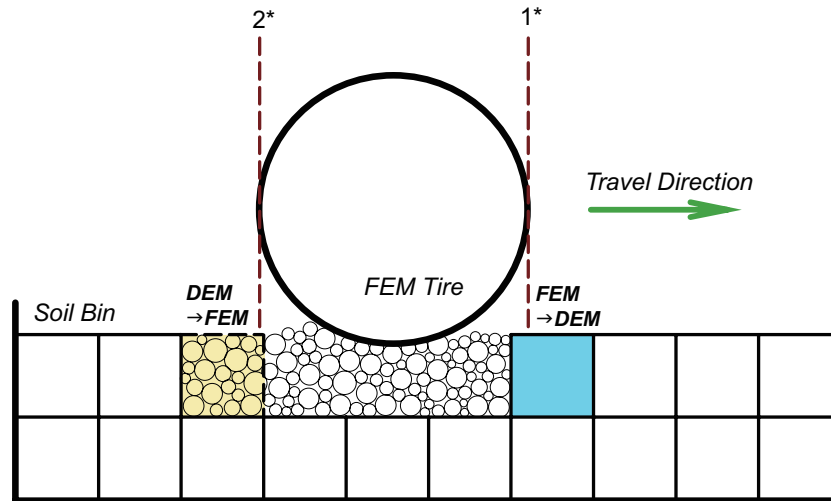


Figure 5-1: Idea behind finite element-discrete element method (FE-DEM) with element conversion.

The simulation of tractive performance comprises the following three modes of computation in FE-DEM: (i) consolidation of soil due to the weight of soil DEs within the soil bin; (ii) free sinkage of tire FEs onto the soil surface until the vertical contact reaction of the tire reaches the contact load of the tire; and (iii) tire travel mode with forced slip with prescribed angular and translational velocities. It should be noted that the conversion of elements should be applied whenever the tire arrives at the elemental boundary in (iii) tire travel mode.

5.1.2 Conversion from FEM to DEM

As shown in Figure 5-1, conversion from FEM to DEM should be activated when the front end of the tire indicated by “1*” extends beyond the left-hand edge of the neighboring FE in front of the tire as shown in blue in Figure 5-1.

When the tire approaches the target FEM element, deformation of the element may be induced. Therefore, each boundary line segment of the target FE defined by the successive boundary nodes of 1–4 will also be deformed accordingly as in Figure 5-2. After deformation of the FE, all nodes in Figure 5-2 (a) will be displaced to new elemental coordinates in Figure 5-2 (b) as

$$\mathbf{x}' = \mathbf{x} + \mathbf{u}, \quad (5.1)$$

where \mathbf{x}' signifies the new elemental coordinate vector of nodes after the deformation, \mathbf{x} denotes the initial coordinate vector of nodes before the deformation, and \mathbf{u} represents the displacement vector.

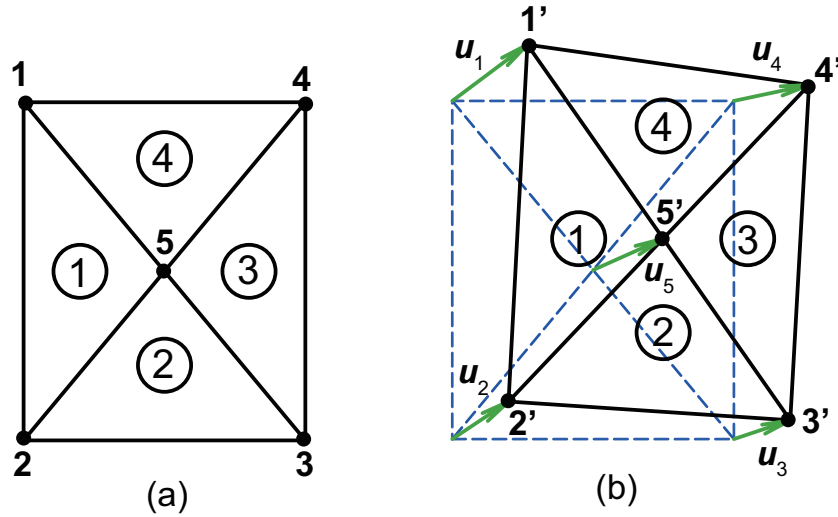


Figure 5-2: Deformation of finite element (FE): (a) before deformation and (b) after deformation.

As for the center of gravity of the isoparametric element (point 5 in Figure 5-2 (a)), its coordinates and displacement can be calculated as

$$\mathbf{x}_5 = \frac{\sum_{i=1}^4 \mathbf{x}_i}{4}, \quad (5.2)$$

$$\mathbf{u}_5 = \frac{\sum_{i=1}^4 \mathbf{u}_i}{4}. \quad (5.3)$$

In these equations, \mathbf{x} and \mathbf{u} denote the coordinate vector and displacement vector, respectively. Each subscript represents the location of the node (right-hand side) or the center of gravity for the element (left-hand side). For simplicity, the shape functions of triangular sub-elements from ① to ④ in the figure can be applied to specify the deformation of an arbitrary point within the triangular sub-element by way of the shape function expressed by the area coordinate within the triangular sub-element.

Therefore, when the DEs are prepared within the FE as shown in Figure 5-3 (a) and the coordinates of the DEs are specified, each DE can be traced based on the shape function of the triangular FEM sub-element. After deformation of the FE expressed by Eqs. (5.1)–(5.3), the displacement of each DE can be traced using the shape function of the triangular sub-element with the deformation of the FEM, as shown in Figure 5-3 (b).

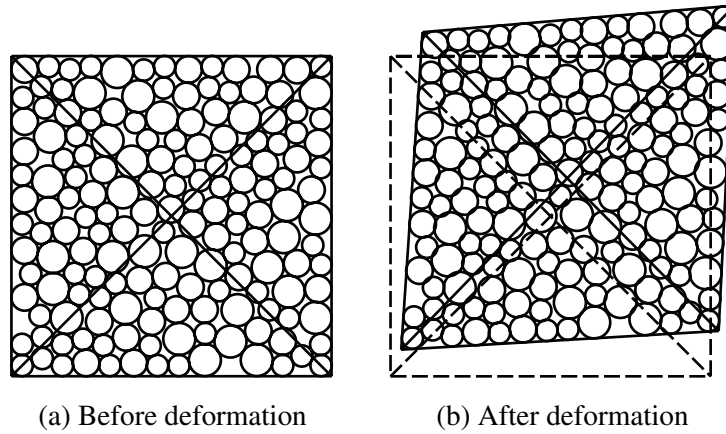


Figure 5-3: Example of elemental deformation using DEs within an FE.

5.1.3 Conversion from DEM to FEM

The conversion from DEM to FEM should be activated when the rear end of tire (indicated by “2*” in Figure 5-1) extends beyond the right-hand boundary of the assigned zone in which the regular FE mesh is defined.

Conversion from DEM to FEM is designed based on the regular discretization of the four-node FE mesh applied for the disturbed DEM zone after tire travel, assuming that the region in which the conversion from DEs to FE mesh is applied will not be affected significantly by the stress states within the DEs.

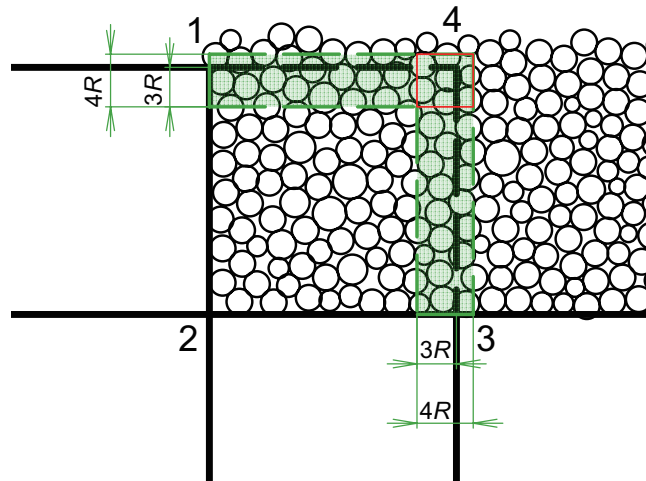


Figure 5-4: Conversion from DEM to FEM.

Let the target DEM zone be located beside the FE meshes and let a new FE be defined with local node numbers 1–4, as depicted in Figure 5-4. It is expected that line segments 3-4 and 4-1

of the FE cannot be defined clearly because the border line for the FEM may not be expressed by a straight line because of the granular nature of the DEs.

In this case, an extended search is applied using the largest radius R of the DEs such that the two straight-line segments 3-4 and 4-1 of the FE consist of an inner zone of thickness $3R$ and an outer zone of thickness R as in Figure 5-4.

The DEs within this border zone are then changed in their role from standard freely moving DEs to attached elements on the line segments of the generated FEM because excessive overlaps might be detected for these DEs when the contacts with the line segments of the FEM are examined. The computational aspects of the attached DEs will be explained further in the next subsection.

It is noteworthy that the new FE should be defined with a consistent pre-stressed condition as a result of the stress and strain states defined by the DEs under investigation for conversion. In this study, however, we apply simple generation of a new FE with no stress delivered from the DEM is applied because the main purpose of this study is to observe the effect of element conversion on the reduction of computational load in FE-DEM.

5.1.4 Attached discrete elements on the border of finite element after tire travel

Attached DEs are introduced to conserve the boundary shape after interaction with the tire in the generated soil FE. Consequently, they have special characteristics of no elemental mass or density. Therefore, there is no effect of gravitational load.

Attached DEs of two types are introduced in this study: (i) attached on a line segment and (ii) attached at a node.

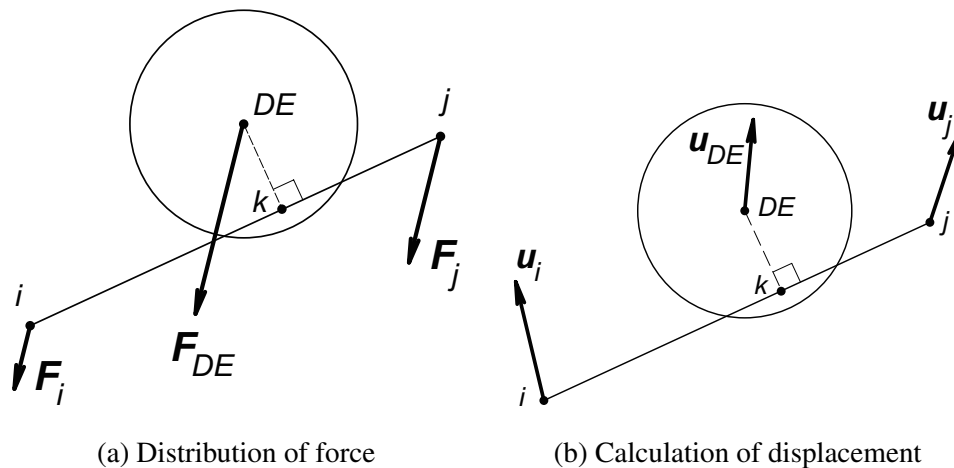


Figure 5-5: Attached DE on a line segment of an FE.

Figure 5-5 shows the case of an attached DE on a line segment of the FEM. Reaction F_{DE} acting on the DE attached to the line segment (see Figure 5-5 (a)) can be distributed to a nodal

reaction using the shape function on the line segment such that the following relationships hold:

$$\mathbf{F}_i = N_i \mathbf{F}_{DE}, \quad (5.4)$$

$$\mathbf{F}_j = N_j \mathbf{F}_{DE}. \quad (5.5)$$

In these equations, $N_i = l_{kj}/l_{ij}$, $N_j = l_{ik}/l_{ij}$, and l_{ij}, l_{ik}, l_{kj} are the lengths on the line segment, where i and j are FE nodes whereas point k is the attached point of the DE on the line segment, and the symbol l_{ik} implies the length of the line segment between i and k .

Similarly, in the case of displacement as in Figure 5-5 (b), the displacement of the attached DE can be specified using two nodal displacements of \mathbf{u}_i and \mathbf{u}_j using the same shape function defined at the attached point k shown above:

$$\mathbf{u}_{DE} = N_i \mathbf{u}_i + N_j \mathbf{u}_j. \quad (5.6)$$

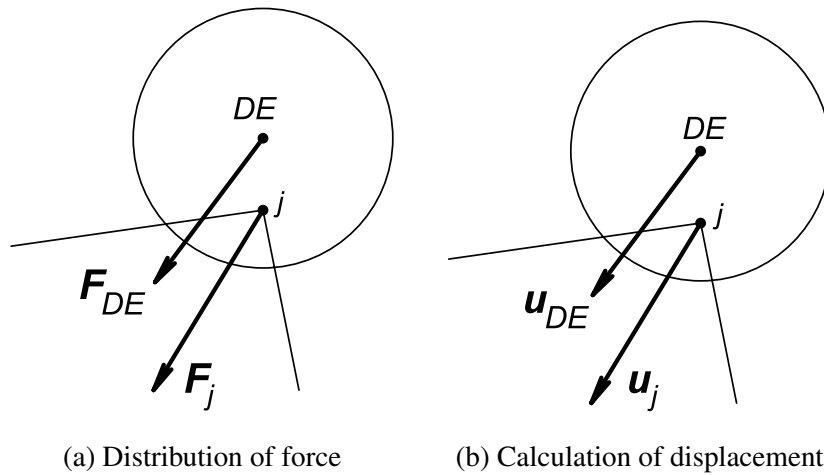


Figure 5-6: Attached DE on FE node j .

For the attached DE to a node, the reaction on the attached DE acts directly on the attached node j of the FEM as in Figure 5-6 (a), such that

$$\mathbf{F}_j = \mathbf{F}_{DE}. \quad (5.7)$$

By substituting $N_i = 0$ and $N_j = 1$ into Eq. (5.6), the displacement of the attached DE shown in Figure 5-6 (b) can be expressed as

$$\mathbf{u}_{DE} = \mathbf{u}_j. \quad (5.8)$$

5.1.5 Preparation of discrete elements for conversion from FEM to DEM

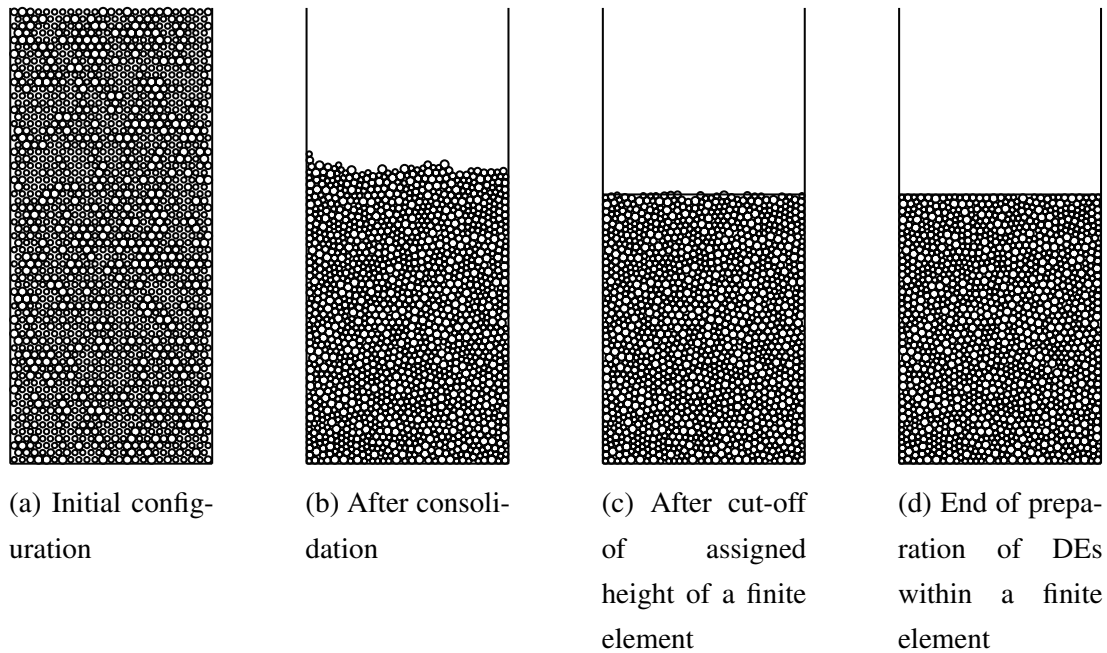


Figure 5-7: Preparation of DEs

Data for an assembly of DEs in an FE should be prepared beforehand. The procedures used in this study were, first, that the same length of soil box as that in the target FEM should be prepared. The DEs were generated inside this box with closest packing using the largest elemental radius (see Figure 5-7 (a)). Second, consolidation of the DEs was applied for 0.5 s with a reduced mass of 1/100 and a coefficient of friction of 0.0 with the smaller time step of 5.0×10^{-7} s. The reason for paying special attention to reducing the mass was to avoid compacting the DEs excessively with their gravity force to maintain the same initial conditions of no deformation by body force for external loads for both the FEs and DEs. The shape of the assembly of DEs is shown in Figure 5-7 (b).

After consolidation, the FE height was adjusted by removing surplus generated DEs (see Figure 5-7 (c)). Because the FEM height was checked based on the DEM elemental coordinates, an irregularly shaped boundary might have occurred at the top face of the assembly. By defining an additional wall at the FEM elemental height, further consolidation was applied for 0.5 s to accommodate the assembly of DEs smoothly within the defined FE. The final shape of the assembly of DEs within the boundary of the FE is depicted in Figure 5-7 (d). The bulk density of the DEs as defined by the boundary lines in Figure 5-7 (d) was used as the FEM elemental density.

The DE coordinates within the target FE were stored so that the information about the generated DEs was available when the conversion from FEM to DEM was activated in iFE-DEM.

5.1.6 Confined compression test for determining Young's modulus of soil FEM

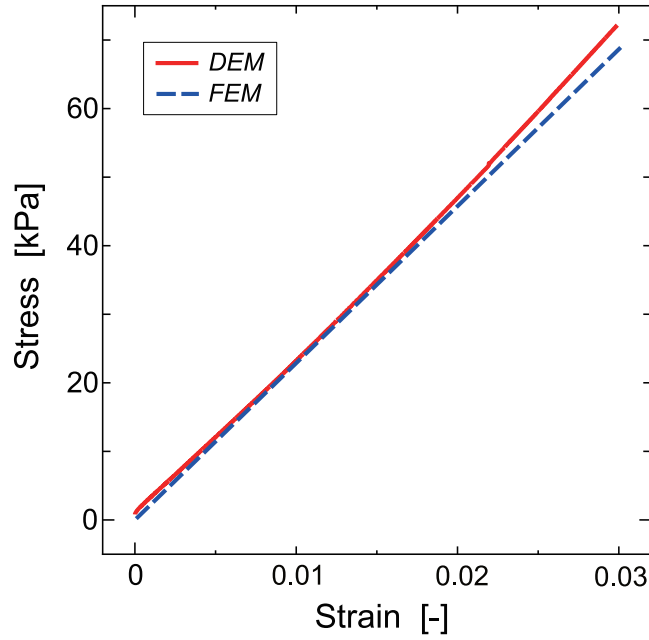


Figure 5-8: Comparison of FEM and DEM under uniaxial confined compression.

To ascertain the Young's modulus for the FEM, a confined compression test was applied as described in an earlier report [1]. For the test, we used one FE and DEs prepared in Figure 5-7 (d). A compressive force was applied to the specimen to obtain a compressive strain of 3%. We selected a maximum compressive strain of 3% considering that the DEM response exhibited a nonlinear curve, and thus tended to deviate from the FEM's straight line response if a larger compressive strain limit was introduced. A compressive strain as small as 3% is also found in the reference [1]. In the FEM, we neglected the volumetric force of gravity. The resulting stress-strain relationship is shown in Figure 5-8. The FEM and DEM results show a similar response, from which the value of $E = 1.7$ MPa was found for the Young's modulus of the soil FEM from the following relation [1].

$$E = E' \frac{(1 + \nu)(1 - 2\nu)}{(1 - \nu)}, \quad (5.9)$$

where E' represents the Young's modulus under confined conditions obtained as the gradient in Figure 5-8 and ν is Poisson's ratio such that $\nu = 0.3$.

The average stress of a DE is defined using the contact reactions as

$$\bar{\sigma}_{ij} = \frac{1}{V} \sum_{m=1}^{n_c} r_i^m F_j^m, \quad (5.10)$$

where V is the element volume, n_c is the number of contacts with the surrounding element, r_j^m signifies the position vector of the contact point from the centroid of the target element, and F_j^m denotes the vector of the contact reaction acting at the contact point [2].

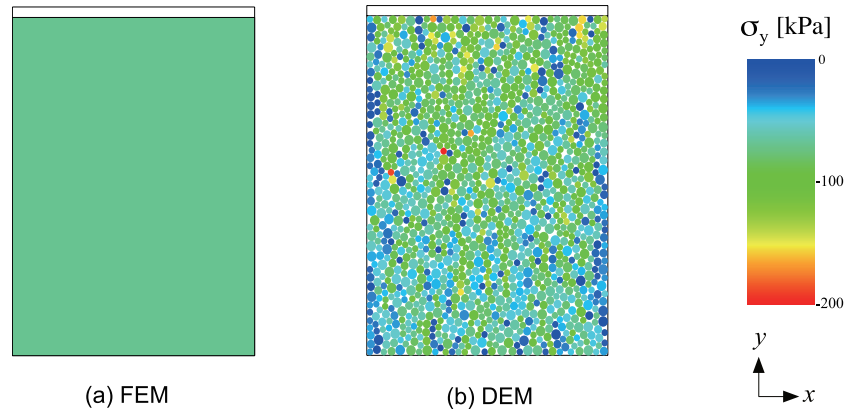


Figure 5-9: Stress distribution in confined uniaxial compression: (a) FEM and (b) DEM.

The state of vertical stress σ_y within the FE and the equivalent stresses of the DEs are portrayed in Figure 5-9, where compressive stress is negative. The FE stress is expressed approximately at the centroid of the FE. Although the DE presents various levels of stress (see Figure 5-9 (b)), the average value of stress σ_y under a vertical compression of 6 mm was found to be similar level in both models, namely -67 kPa (FEM) and -69 kPa (DEM).

5.1.7 Tractive performance

The tractive performance of the tire can then be obtained from the torque and drawbar pull predicted from FE-DEM with PID control models. The slip of the tire is defined as Eq. (3.8). The measures for assessing the tractive performance is summarized in Eqs. (3.5) - (3.7), which can be obtained from the result of PID traveling control.

5.2 Numerical experiment

5.2.1 FE-DEM parameters

The nominal size of the tire modeled was 165/60R13, with a diameter of 535 mm and a width 170 mm, which is the same as the tire used by Shinone et al. [7] in a previous experiment. The tire was driven with a constant circumferential velocity of 97.6 mm/s and a vertical contact load of 980 N, with an inflation pressure of 140 kPa. The tire was found to be in rigid contact under the given loading conditions.

The tire model is an FEM with 155 nodes and 140 elements. Figure 5-10 shows the tire mesh configuration in three parts: the wheel rim, the intermediate layer which represents air, and the surface layer for the tread.

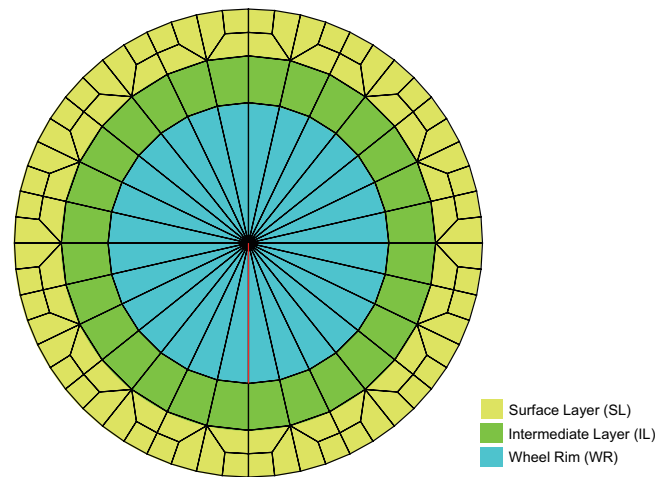


Figure 5-10: FEM tire model.

Table 5-1: Tire FEM Model Parameters

	WR	IL	SL
Young's modulus [MPa]	200.0	0.3	1.5
Poisson's ratio [-]	0.3	0.49	0.49
Element density [kg/m ³]	3000.0	1000.0	1000.0
Width [m]	0.01	0.17	0.17
Damping coeff. [N·s/(m·kg)]	1.0	1.0	10.0

NB) WR, wheel rim; IL, intermediate layer; SL, surface Layer

Table 5-2: Parameters for the soil FEM model

Number of FEs	32
Number of FEM nodes	51
Young's modulus [MPa]	1.7
Poisson's ratio [-]	0.3
Length of unit FE [m]	0.15
Height of unit FE [m]	0.2
Elemental density [kg/m ³]	2200
Friction coefficient between FE-DE	0.6
Length of soil bin [m]	2.4
Travel distance [m]	0.7
Averaging distance [m]	last 0.3

Table 5-3: Parameters for DEM and FE-DEM

	DE-DE	DE-Wall	DE-FE
Normal spring const. [N/m]	5.0×10^5	5.0×10^5	5.0×10^5
Tangential spring const. [N/m]	1.25×10^5	1.25×10^5	1.25×10^5
Friction coeff. [-]	0.6	0.4	0.5
Friction coeff. at consol. [-]	0.0	0.0	NA

Table 5-4: Parameters for the PID model in FE-DEM

PID Term	Proportional	Integral	Derivative
Drawbar pull	1.0×10^6 [N/m]	1.0×10^4 [N/(ms)]	1.0×10^4 [N s/m]
Torque	1.0×10^5 [Nm/rad]	1.0×10^3 [Nm/(rad s)]	1.0×10^3 [Nm s/rad]

Other parameters are listed in Table 5-1–5-4. Eight slip levels were selected in the computation of the tractive performance of the tire from 0%–70% with an increment of 10%. The DEs used in the model were a mixture of three circular elements with radii of 2 mm, 2.5 mm, and 3 mm with the ratio of 3:2:1 by number.

The contact model parameters in Table 5-3 were the same as those used for FE-DEM traction analysis for the target tire [6], where tire deformation is assumed to not occur by the increase of spring constants from the previous FE-DEM for an elastic wheel in Chapter 3. We determined the PID parameters, which are listed in Table 5-4 by considering a larger contact load in the current analysis than was considered in the previous elastic wheel analysis [6].

The total numbers of DEs in the initial setup of the tire-travel mode are listed in Table 5-5. In case of the small DEM region, the target soil ranging from a block just beneath the left edge of the tire to the one just beneath the right edge are assigned as DEM elements. For the middle DEM region, two more DEM blocks are added to the small DEM region model from the FEM elements, one in the forward and another in the rearward direction of the tire. Similarly, one more outside soil DEM block from the FEM elements is added to the large DEM region. The DEM only soil model was the case in which only the DEM was used without introducing the FEM. The height of each FE for the soil model was set as 0.2 m, which was slightly less than the tire radius. The number of DEs and corresponding FEs may be changed depending on the tire's rolling center location in the model region.

Table 5-5: Total number of DEs at the start of tire-travel analysis

Small DEM region	Middle DEM region	Large DEM region	DEM only
7255	10157	13059	46280

5.2.2 Program flow for iFE-DEM

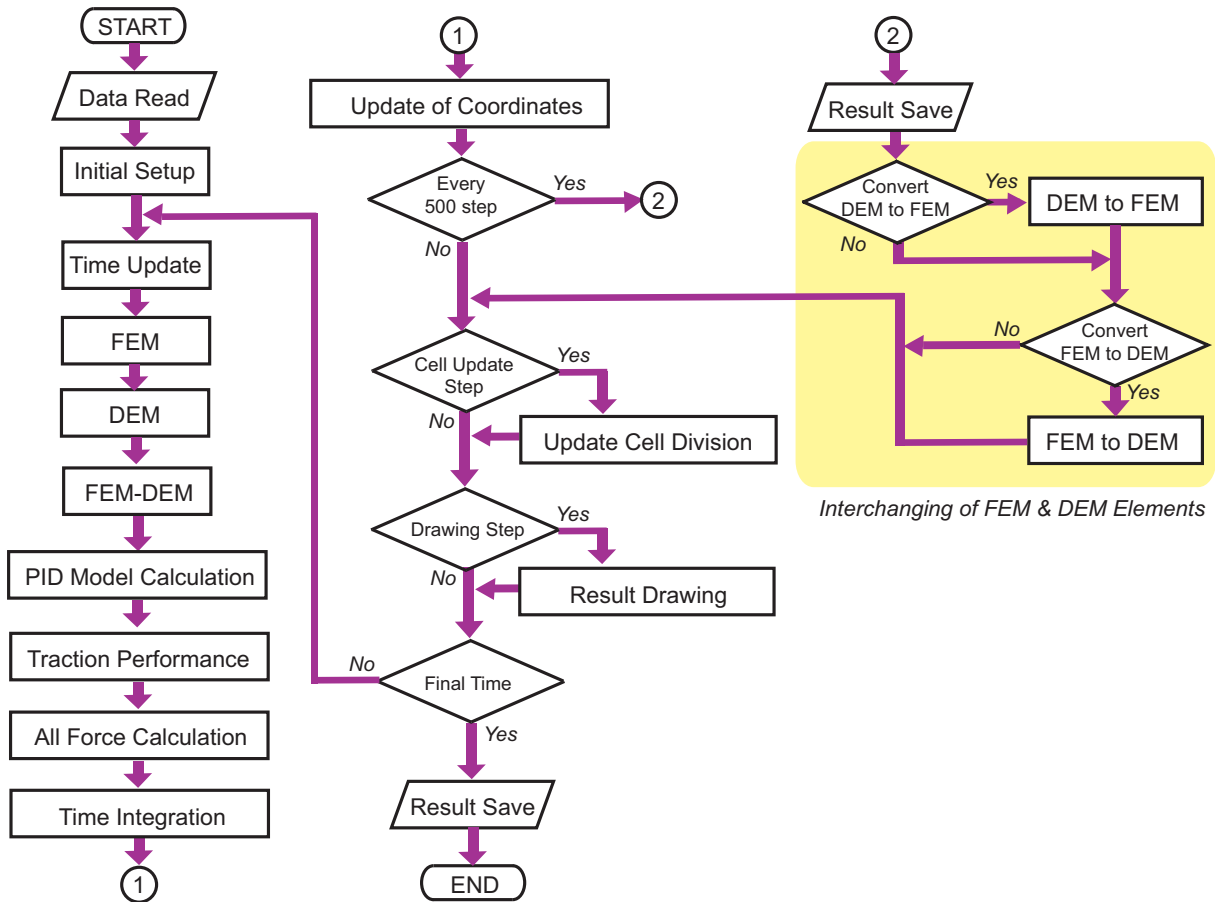


Figure 5-11: Schematic flow of iFE-DEM program for tire travel analysis.

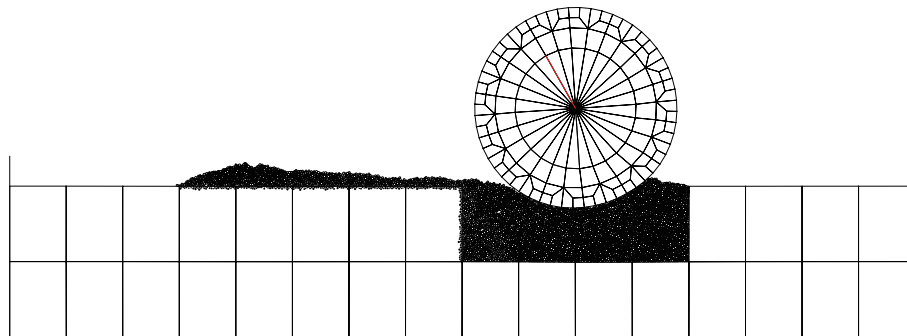
Our in-house computer program for the 2D FE-DEM with PID-controller models was updated to include interchangeable modeling between DEM and FEM for the soil model.

The program flow for the tire travel analysis is shown schematically in Figure 5-11. The algorithm for interchangeable modeling is implemented after the coordinate update procedure.

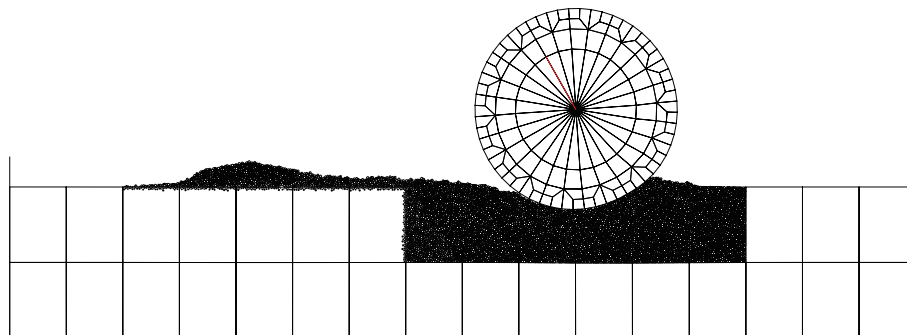
The conversion is activated after every 500 time steps of numerical integration of the equations of motion. In the current program, the switch to start conversion is based on the travel distance of the left-hand and right-hand outermost vertical edge lines of the tire (Figure 5-1). As shown in Section 5.1, the right-hand edge of the small region of the DEM is set as the basis of the conversion from FEM to DEM. Similarly, the switch to start changing from DEM to FEM at the DEM region behind the tire turns on whenever the left-hand outermost edge line of the tire travels the length of the FE that can be generated on the DEM elements.

5.3 Results and discussion

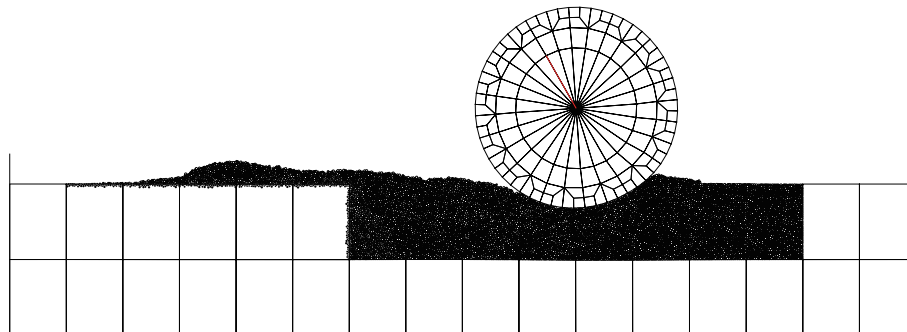
5.3.1 Soil deformation under tire travel



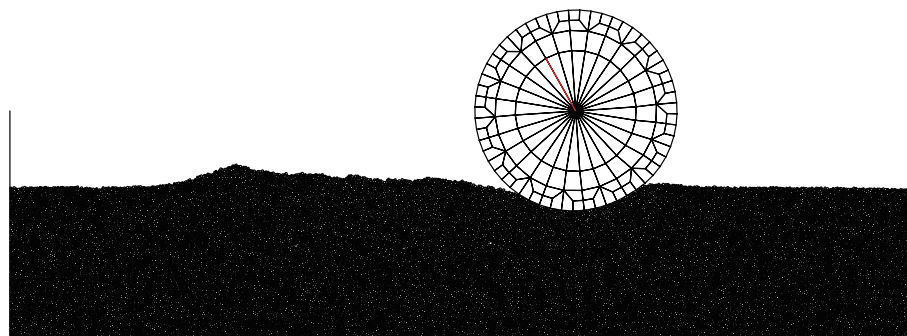
(a) Small DEM region



(b) Middle DEM region



(c) Large DEM region



(d) DEM only soil model

Figure 5-12: Examples of soil deformation at the end of tire travel with a slip of 70% in iFE-DEM.

Figure 5-12 presents the results from iFE-DEM for a slip of 70% with different sizes of DEM for (a) the small DEM region, (b) the middle DEM region, (c) the large DEM region, and (d) the DEM only soil model. Soil upheaval in front of the tire in the surface profile of the DEM region can be observed similarly in cases of Figure 5-12 (a), (b), and (c). However, such clear upheaval cannot be seen in the DEM only soil model in Figure 5-12 (d).

The soil upheaval, shown in Figure 5-12(a)-(c), was caused by the insufficient space against the preceding soil FE depending on the FEM-to-DEM conversion timing, where the approaching tire will intensify the forward flow of soil DEs within the short length against the soil FE boundary.

In Figure 5-12, the soil surface profile as traced after the tire travel in all cases can be regarded as similar, which implies that the idea of an attached DEM in the iFE-DEM is an effective one.

5.3.2 Tractive performance

The iFE-DEM results for tractive performance are shown in Figure 5-13 for (a) the small DEM region, (b) the middle DEM region, and (c) the large DEM region. The results from the DEM only soil model are shown for comparison in Figure 5-13 (d).

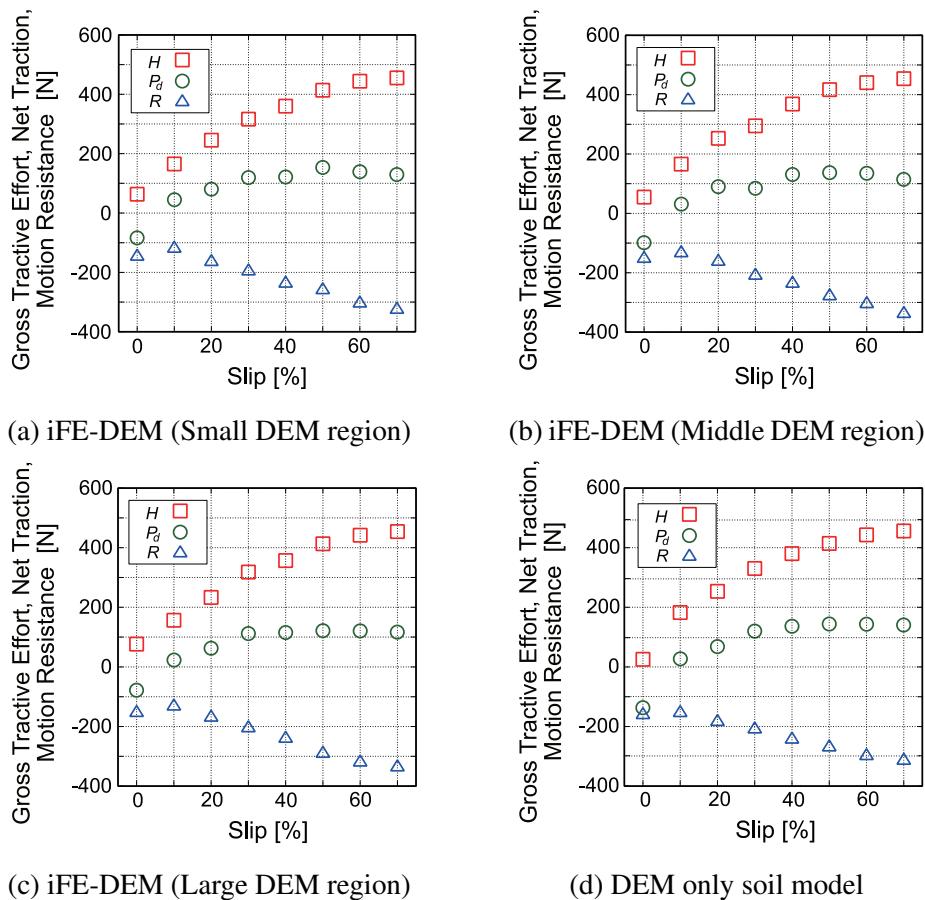


Figure 5-13: Comparison of tractive performance.

As the initial size of the DEM region in the iFE-DEM increases, the results for tractive performance clearly approach those of the DEM only analysis. Clear differences are evident at small slips of 0% and 10%.

Compared to the previous experimental results [7], the gross tractive effort becomes slightly small at a slip of 0% in all cases of DEM regions in Figure 5-13. Zero net traction can be expected at a slip of roughly 7%, which also corresponds to the previous experimental results [7]. The net traction shows similar values for all slip condition, although slight fluctuations can be seen in the results for the small and middle regions.

The iFE-DEM results for tire sinkage are shown in Figure 5-14 for (a) the small DEM region, (b) the middle DEM region, and (c) the large DEM region. Moreover, the results from the DEM only soil model are presented for comparison in Figure 5-14 (d).

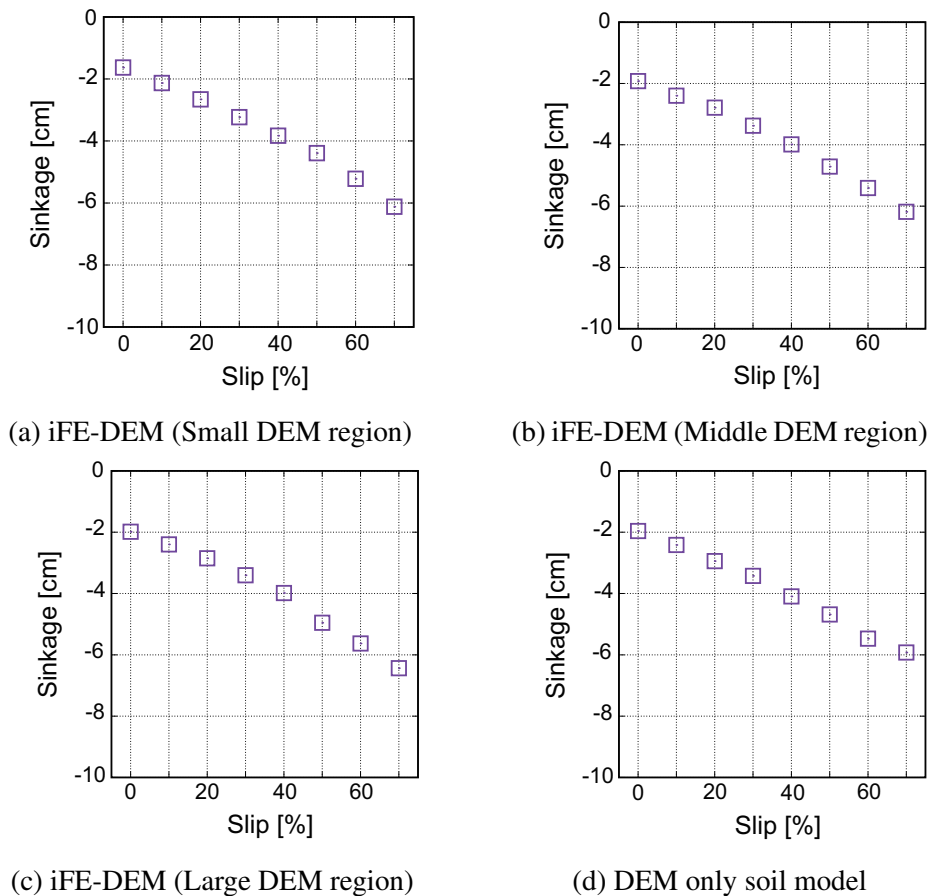


Figure 5-14: Comparison of tire sinkage.

We calculated the tire sinkage as the difference between the height of the tire rotation center during tire travel and momentarily before the tire was contacted to the soil surface. Using this definition of sinkage, we could include not only the tire model deflection, but also the deformation of soil FEs and DEs.

The tire sinkage differs among the cases, but the results can be regarded as similar as seen in

Figure 5-14.

5.3.3 Computational load in iFE-DEM

We measured the elapsed times for the four cases of the DEM regions listed in Table 5-5. All computations were executed by a PC-based Linux computer (Core i7 5960X, 3 GHz; Intel Corp.) with a main memory of 32 GB. Parallel processing such as OpenMP was not applied in the current iFE-DEM. The initial configuration of the FE-DEM was prepared beforehand. The computational time was measured only for the travel analysis of the tire on the soil model. The results for the middle slip condition of 40% are depicted in Figure 5-15.

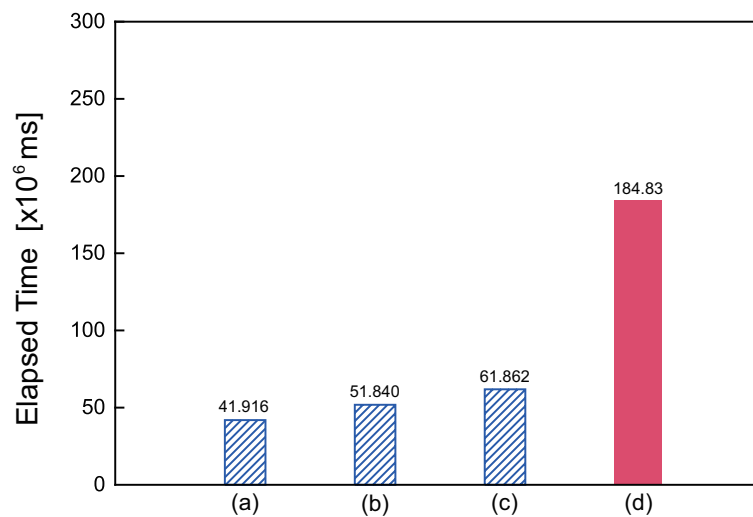


Figure 5-15: Computational loads of iFE-DEM: (a) small DEM region, (b) middle DEM region, (c) large DEM region, and (d) DEM only

To evaluate the reduction of computational time with the iFE-DEM, we calculated the ratio of the iFE-DEM computational time to that of the FE-DEM with the DEM only soil model for three region sizes. The small DEM region shows the greatest reduction of computational time, with a ratio of 0.23; the middle DEM region yields 0.28 and the large DEM region yields 0.33. It is noteworthy that although the elapsed time of computation depended on the distance traveled in each slip, the ratio of computational time did not show significant variation with slip in the preliminary observation.

Consequently, from Figure 5-15, we confirm that the introducing the iFE-DEM is effective and that it helps to reduce the computational time to as little as 23% in the case of the small DEM region for a slip of 40% against the FE-DEM analysis with the DEM only soil model.

5.3.4 Stress distribution within soil model in iFE-DEM

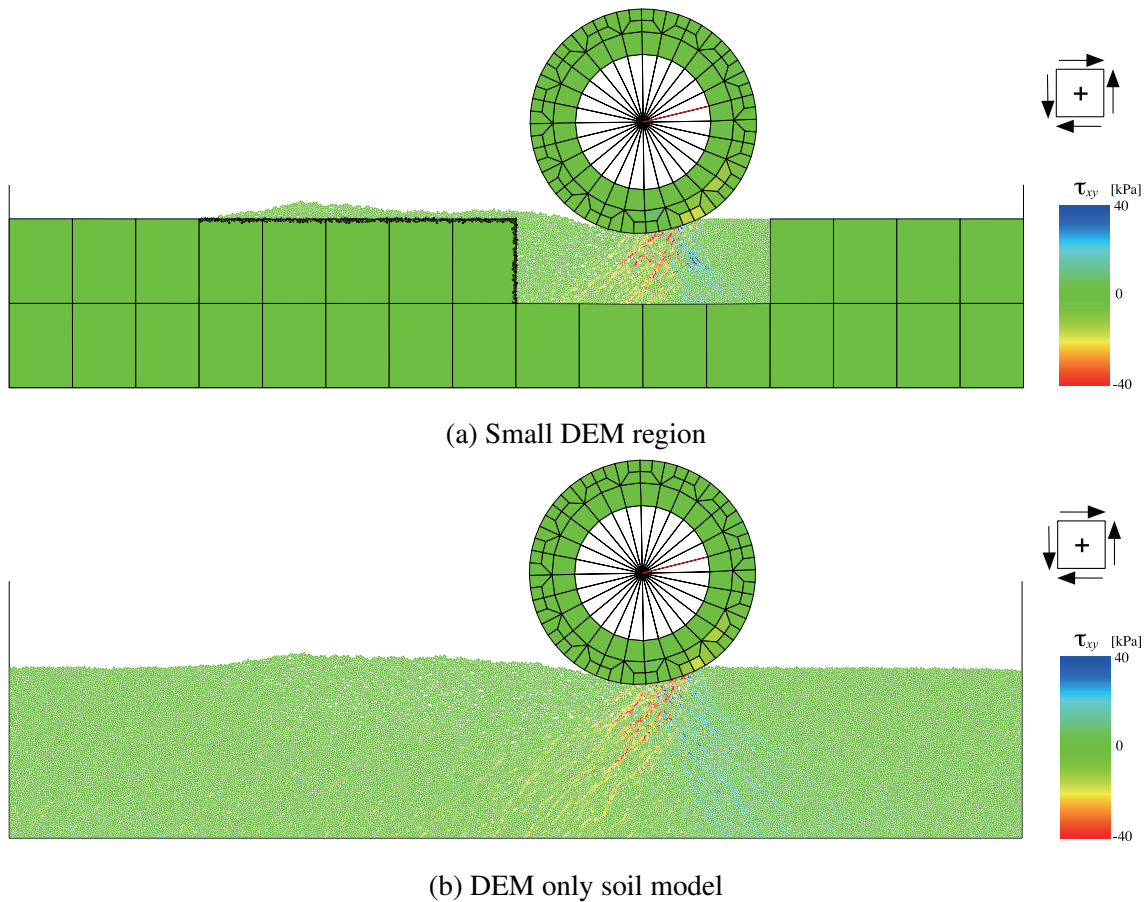


Figure 5-16: Examples of shear stress distribution at the end of tire travel with a slip of 40%.

Because the traction performance depends on the shear stress within the soil, the distribution of shear stress is calculated based on Eq. (5.10) for the DEM and on elemental averaging in the FEM. Regarding the tire, shear stress is calculated everywhere except at the wheel rim. Figure 5-16 presents examples of the shear stress distribution within the model for the cases of the small DEM region with the FEM (Figure 5-16 (a)) and the DEM only soil model (Figure 5-16 (b)) with a slip of 40%. Figure 5-16 also shows the direction of the positive shear stress.

The shear stress distributions under the tire in the soil DEM model in Figure 5-16 (a) and (b) become similar, where large negative shear stress is distributed backward from the contact surface in advance of the rotation center of the tire. After passage of the tire center of rotation, the shear stress becomes much smaller in both cases. Moreover, concentration of positive shear stress is apparent in Figure 5-16 (a).

However, from Figure 5-13 (a) and Figure 5-13 (d), the difference in travel performance at a slip of 40% is apparently not so large. Thus, the effect of no succession of stress at the time of element conversion may be neglected coincidentally as the first approximation in the analysis of tire

traction performance as in this study. However, further investigation of stress succession in iFE-DEM should be conducted for detailed stress analysis within the soil model.

5.4 Conclusion

This study assessed a new FE-DEM for soil-tire interaction with interchangeable modeling between FEM and DEM (iFE-DEM) for tire traction performance analysis. The iFE-DEM method models the soil initially in a soil bin using an FEM, except for the region under or near the tire, which is modeled using a DEM.

The results of the iFE-DEM analysis revealed that faster computation could be realized by reducing the extent of the initial soil DEM. Moreover, when the smallest region of soil DEM was used, the computational time was as little as 23% of that using FE-DEM with the DEM only soil model for a slip of 40%. All the results of iFE-DEM traction analysis using small, middle, and large soil DEM models resembled those obtained using FE-DEM with the DEM only soil model.

The effectiveness of iFE-DEM analysis was demonstrated in this study, but the optimum sizes of the unit FE and the initial DEM region should be investigated further based on the parametric analysis. Although the numerical analysis was conducted in two dimensions, the iFE-DEM could be applied to a lugged tire in three dimensions by extending the FEM and DEM to more degrees of freedom. Moreover, it is necessary to use cohesive soil in the DEM because of the possibility of different stress distributions in soil as shown numerically in an earlier report [3], which might affect the applicability of the proposed iFE-DEM. We also recommend conducting a detailed investigation of an equivalent stress state and succession of stress within the soil model before and after element conversion to refine the proposed iFE-DEM further and make it applicable to various interaction problems of terramechanics.

Appendix

As for iFE–DEM, to better understand the relationship between soil FEs and DEs in a defined region listed in Table 5-5, we depict an example of tire travel from beginning to end in Figure 5-A.1. The figure summarizes the case of large DEM region with a 40% slip. As shown in Figure 5-A.1, with the conversion from FEM to DEM or vice versa, the designed model DEM region expands or shrinks accordingly.

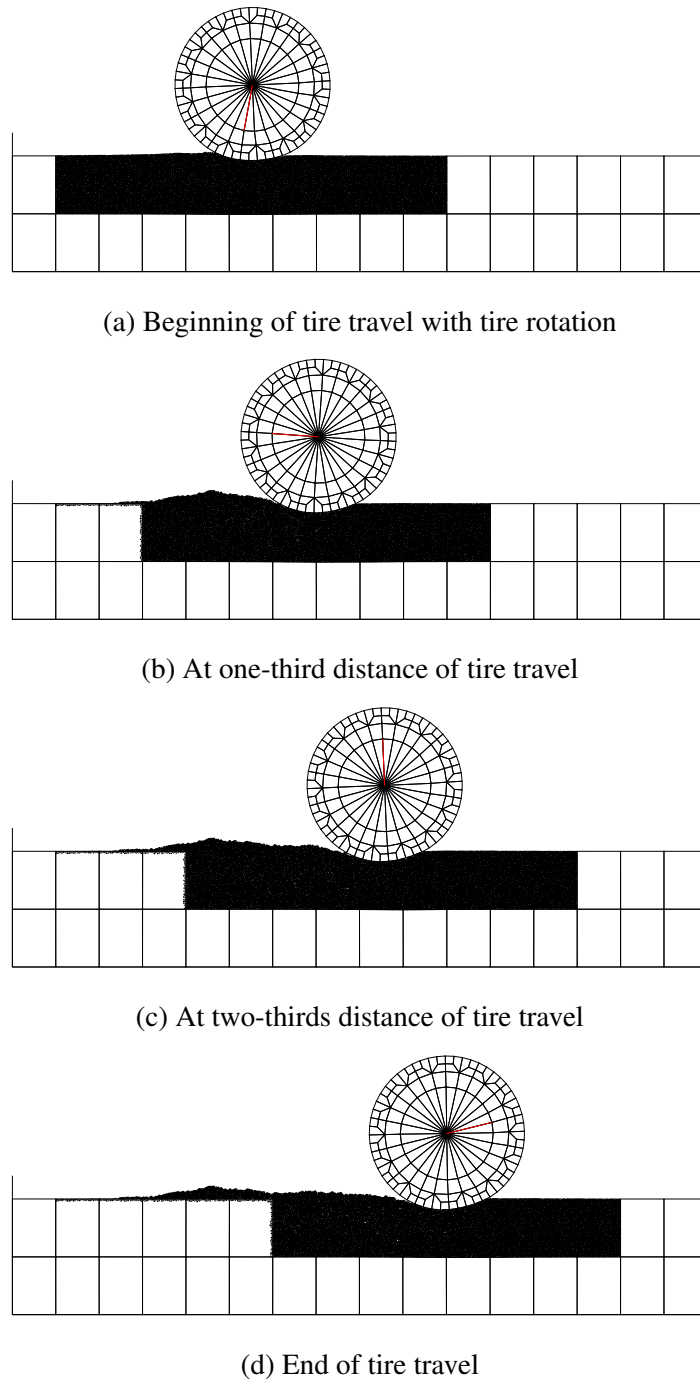


Figure 5-A.1: Example of tire travel for a case of large DEM region with a slip of 40% in iFE-DEM.

References

- [1] Coetzee, C. J. and D. N. J. Els. 2009. Calibration of granular material parameters for DEM modelling and numerical verification by blade-granular material interaction. *Journal of Terramechanics* 46: 15-26.
- [2] Drescher, A. and G. de Josselin de Jong. 1972. Photoelastic verification of a mechanical model for the flow of a granular material. *Journal of the Mechanics and Physics of Solids* 20: 337-351.
- [3] Fervers, C.W., 2004. Improved FEM simulation model for tire–soil interaction. *Journal of Terramech.* 41 (2/3), 87–100.
- [4] Nakashima, H. and Y. Takatsu. 2008. Analysis of tire tractive performance on deformable terrain by finite element–discrete element method. *Journal of Computer Science and Technology* 2(4), 423-434.
- [5] Nakashima, H., Y. Takatsu, H. Shinone, H. Matsukawa, and T. Kasetani. 2009. FE–DEM analysis of the effect of tread pattern on the tractive performance of tires operating on sand. *Journal of Mechanical Systems for Transportation and Logistics* 2 (1): 55-65.
- [6] Nishiyama, K., 2016. FE-DEM Simulation of Tire Performance on a Dry Sand Terrain (Unpublished Master Thesis). Division of Environmental Science & Technology, Graduate School of Agriculture, Kyoto University (in Japanese).
- [7] Shinone, H., H. Nakashima, Y. Takatsu, T. Kasetani, H. Matsukawa, H. Shimizu, J. Miyasaka, and K. Ohdoi. 2010. Experimental analysis of tread pattern effects on tire tractive performance on sand using an indoor traction measurement system with forced-slip mechanism. *Engineering in Agriculture, Environment and Food* 3(2): 61-66.

Chapter 6

Conclusions

The purpose of this study was to develop a new framework of FE–DEM for evaluating the tractive performance of a tire on dry sand with a high accuracy, while reducing the computational cost of DEM. From the studies described in Chapters 3–5, the following three points were clarified.

In Chapter 3, the 2D FE–DEM code was updated by introducing a PID controller model that allowed achieving the same evaluation procedure as that of the equivalent experiments. The tractive performance of elastic iron wheels with different rigidities developed for the Mars rover of the European Space Agency as a prototype was analyzed, and it was confirmed that the accuracy of the simulation, especially the relationship between slip and motion resistance, can be improved. Moreover, the tractive performance of these wheels under Mars’s gravity was predicted. It was estimated that two prototype wheels with different rigidities would result in a similar tractive performance on the surface of Mars.

In order to expand the application scope of the developed 2D FE–DEM, it was demonstrated in Chapter 4 that the normal and tangential contact stresses can be calculated using a simple averaging method, assuming stationary travel of a tire and the rigid contact mode. Moreover, the tractive performance can be obtained using a semi-empirical (or parametric) method that integrates stress distributions over the contact surface of a tire with soil. The obtained tractive performance using such a parametric analysis was confirmed to be similar to that obtained from the 2D FE–DEM with a PID controller model and the previous experimental results.

In Chapter 5, a new FE–DEM with interchangeable modeling (iFE–DEM) for tire traction analysis was proposed to reduce the computational cost. In essence, iFE–DEM applies elemental conversion from FE to DE or from DE to FE to reduce the influential region of soil under a traveling tire to a small DEM region, while keeping the remaining region of the soil model in FEM. The tractive performance of a tire predicted using iFE–DEM was found to be similar to that of the already existing FE–DEM with a PID controller model using the DEM-only soil model. Furthermore, it was clear that a reduction of 77% in the elapsed time of iFE–DEM computation could be achieved when a small DEM region was applied.

Therefore, it can be concluded that a more accurate, faster simulation tool for wheel–soil interaction problems was realized in this study. The developed 2D FE–DEM with a PID controller model and iFE–DEM can surely contribute to visualizing the complicated phenomena encountered during soil-tire interactions. They can also help tire researchers and/or engineers predict and optimize the tractive performance of off-road tires.

While adequately precise results can be obtained using the current 2D analysis as shown in this dissertation, introducing a 3D method for FE-DEM and investigating the effect of the third dimension can be performed as part of future work. When realizing 3D FE–DEM, parallel processing utilizing the General-Purpose computing on Graphics Processing Units (GPGPU) should be taken into consideration. Once both 2D and 3D FE–DEM are developed, a further discussion can be initiated on which dimensions of analysis should be included in a numerical tool to provide fast and accurate predictions of the soil-tire interaction from the engineers' viewpoint.